Continuous Production of CO from CO_2 by RWGS Chemical Looping in Fixed and Fluidized Bed Reactors

Marcus Wenzel[a,*], Liisa Rihko-Struckmann[a], Kai Sundmacher[a,b]

[a] *Max-Planck-Institute for Dynamics of Complex Technical Systems, Sandtorstr. 1, 39106 Magdeburg, Germany*
[b] *Otto-von-Guericke-University Magdeburg, Universitätsplatz 2, 39106 Magdeburg, Germany*

Abstract

A fixed bed and a fluidized bed reactor design for the reverse water-gas shift chemical looping (RWGS-CL) process with 80 wt% $Fe_2O_3 - Ce_{0.5}Zr_{0.5}O_2$ as oxygen storage material (OSM) are analyzed and compared by process simulation. The influence of gas inlet flow velocity on the the reaction regime is investigated and feasible regions of operation for continuous CO production are identified. Two performance indicators are defined for the process: 1) the average CO concentration and 2) the OSM utilization. Optimization problems are solved to maximize the performance indicators and analyze their mutual dependency. The results are discussed in a Pareto plot. It is shown that a fixed bed reactor design is advantageous for the RWGS-CL process because of more degrees of freedom for operation compared to the fluidized bed reactor design. A quasi-continuous production of CO is demonstrated for both reactor designs. A steady CO production with an average CO mole fraction of $\bar{x}_{CO} = 0.64$ and an OSM utilization of 83.9% can be realized with two fixed bed reactors. The fluidized bed reactor configuration can potentially minimize problems associated with material sintering but the average CO concentration and OSM utilization are significantly lower compared to the fixed bed due to the limited operational freedom. The results indicate the importance of dynamic simulations for understanding and exploiting the kinetic and thermodynamic aspects of inherently dynamic processes like RGWS-CL to maximize process performance.

Keywords: Reverse water-gas shift, Chemical looping, Fixed bed reactor, Fluidized bed reactor, Dynamic simulation, Optimization

1. Introduction

Syngas is widely used in industry as a building block for the production of many bulk chemicals and chemical intermediates. The H_2/CO-ratio of the syngas is determined by its production method. Low H_2/CO syngas is required in the Monsanto process for acetic acid production and for hydroformylation processes. High H_2/CO syngas is used for alcohol synthesis. Today, syngas is produced almost exclusively

*Corresponding author

from fossil fuels by steam reforming of natural gas or gasification of coal, depending on the desired H_2/CO-ratio. In light of the current and future global challenges associated with the rising CO_2 levels in the atmosphere, traditional processes based on fossil fuels must be substituted to minimize the CO_2 production.

One possible way to mitigate future CO_2 emissions is to use it as the main carbon source instead of fossil fuels. In the context of sustainable syngas production, the reverse water-gas shift (RWGS) reaction is of high importance, as it converts CO_2 to CO with the help of process heat and hydrogen. Using CO_2 and H_2 produced from renewable sources like wind or solar energy, syngas can be produced sustainably (i.e. without fossil fuels). Therefore, the RWGS reaction plays an important role for closing the atmospheric carbon cycle in the future. The RWGS reaction is mildly endothermic and proceeds according to

$$\mathrm{H_2 + CO_2 \rightleftharpoons H_2O + CO} \qquad \Delta H_R(1073K) = 37\,\mathrm{kJ/mol}. \tag{1}$$

By introducing a metal oxide as an oxygen storage material (OSM), the RWGS reaction can be split into a reduction and oxidation reaction. This cyclic two-step process for CO_2 activation is referred to as reverse water-gas shift chemical looping (RWGS-CL). By switching the gas flows between at least two reactors after the OSM is reduced or oxidized, respectively, a quasi-continuous process can be established which is illustrated in Figure 1. This approach leads to efficiency improvements compared to the conventional RWGS reaction because the two-step operation yields partially separated gas streams and thus simplifies downstream gas separation [1]. Efficiency improvements are most pronounced for syngas production with low H_2/CO-ratio. Furthermore, unwanted side reactions can be eliminated by separating the reactants spatially or temporally and favorable thermodynamics can be obtained by choosing suitable oxygen storage materials [2]. In a previous work, a mixed oxide of 80 wt% Fe_2O_3 and 20 wt% $Ce_{0.5}Zr_{0.5}O_2$ was used as OSM for RWGS-CL [3]. The simplified reaction scheme (assuming that the support metal oxide, $Ce_{0.5}Zr_{0.5}O_2$, does not participate in the reactions) is given by equations (2) to (5). Redox reactions are considered to occur only between Fe_3O_4, Fe_O and Fe (the completely oxidized state, Fe_2O_3, is not achievable by oxidation with CO_2).

Oxidation step 1:	$\mathrm{Fe + CO_2 \rightleftharpoons FeO + CO}$	$\Delta H_R(1073K) = 15.12\,\mathrm{kJ/mol}$	(2)
Oxidation step 2:	$\mathrm{FeO + 1/3\,CO_2 \rightleftharpoons FeO_{4/3} + 1/3\,CO}$	$\Delta H_R(1073K) = -3.15\,\mathrm{kJ/mol}$	(3)
Reduction step 1:	$\mathrm{FeO_{4/3} + 1/3\,H_2 \rightleftharpoons FeO + 1/3\,H_2O}$	$\Delta H_R(1073K) = 15.43\,\mathrm{kJ/mol}$	(4)
Reduction step 2:	$\mathrm{FeO + H_2 \rightleftharpoons Fe + H_2O}$	$\Delta H_R(1073K) = 21.72\,\mathrm{kJ/mol}$	(5)

Due to the cyclic switching between two process steps, RWGS-CL is more complex than the traditional RWGS process and a conventional steady-state operation is not possible. However, a cyclic steady-state (CSS) can be achieved after prolonged switching. Many advanced reactor designs have been proposed in the literature for chemical looping processes to deal with the operational difficulties arising from their cyclic

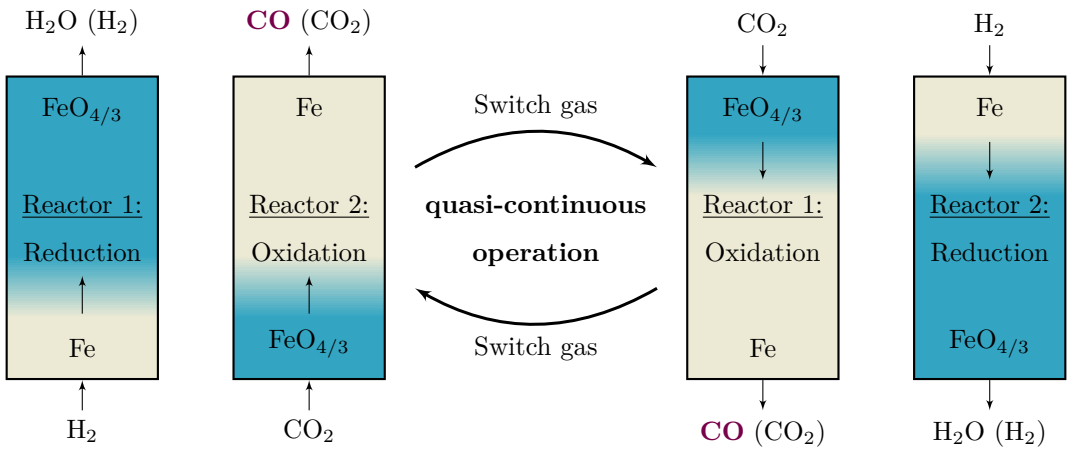

Figure 1: Illustration of the RWGS-CL concept in two fixed bed reactors which are operated simultaneously. After the OSM is exhausted (i.e. reduced or oxidized), the gas inlet composition is switched and the gas flow direction is reversed. Repeated switching yields a quasi-continuous process for CO production. Colors indicate different oxidation states of the OSM: blue=completely oxidized ($FeO_{4/3}$), beige=completely reduced (Fe).

nature and to increase their process efficiency. Cho *et al.* used a continuously operating moving bed chemical looping design with three reactors for the production of hydrogen and electricity [4]. Wei *et al.* investigated a $10\,kW_{th}$ chemical looping gasification plant for biomass based on an interconnected fluidized bed reactor design [5]. For thermochemical looping, Ermanoski *et al.* demonstrated a reactor with a continuously moving bed of particles [6]. Welte *et al.* showed a $2\,kW_{th}$ aerosol reactor using a downward gravity-driven aerosol flow [7]. For chemical looping combustion (CLC) rotating reactors have been proposed by Håkonsen and Blom [8]. While these reactor designs show promising results and avoid some of the challenges associated with conventional reactor designs (e.g. material sintering[9, 10, 11], heat recovery problems), most of them are still far from an industrial scale and face other challenges (e.g. material attrition, controllablity issues, complicated design). Often, conventional reactor designs such as fixed beds and fluidized beds are industrially preferred because of their relative simplicity and well known behavior. Of all chemical looping processes, CLC is arguably the most advanced technology in terms of scale of operation with several larger-scale plants ($50 - 150\,kW_{th}$) being mentioned in the literature [12, 13, 14, 15, 16, 17]. They are all based on interconnected fluidized bed reactor designs. Zhou *et al.* noted that the main problem with fluidized bed reactors is attrition and that it may be avoided by using a fixed bed reactor design [18]. However, in simulation studies they found that the temperature gradients in the fixed bed can become problematic and, therefore, they argued for using fluidized bed reactors for large-scale implementation of CLC. In RWGS-CL, temperature gradients are expected to be a minor problem because the involved reactions are only mildly exothermic or endothermic. Furthermore, a better temperature control can be achieved by using multi-tube reactor designs instead of single-tube reactors. The advantages and disadvantages of fixed bed vs. fluidized

bed reactors must be evaluated in detail for RWGS-CL since not all results from CLC can be safely adopted.

Therefore, a fixed bed and a fluidized bed reactor design for the RWGS-CL process for continuous production of syngas are analyzed in this work to show the possibilities and limitations of using simple, well known reactor designs. The goal is to investigate from a theoretical point of view whether fixed or fluidized bed reactors yield better performance for the RWGS-CL process. With these insights informed decisions can be made on which reactor type warrants further investigation.

Zhang et al. [9] and Zhou et al. [18] compared fixed bed and fluidized bed reactor designs for CLC systems. Zhang et al. performed performed lab-scale experiments and concluded that the fixed bed reactor yields higher carbon conversion for CLC of coal with iron oxide (unmodified) as oxygen storage material. However, they also noted that a fluidized bed reactor type may prove advantageous for long term operation since it effectively avoids sintering and agglomeration [9]. Zhou et al. performed simulation studies for CLC of methane on nickel oxide as oxygen storage material. They state that the fluidized bed reactor is "more appropriate for large-scale implementation of the CLC process because of its uniform temperature and pressure distribution, high CO_2 selectivity ($> 95\%$), negligible carbon formation (< 2mol% C basis), and high fuel conversion ($> 90\%$) over longer reduction periods". [18]. While both studies are concerned with CLC the results and recommendations for reactor selection vary significantly due to several factors (different OSM, theoretical vs. experimental approach, etc.). It is therefore concluded that the selection of a specific reactor design for RWGS-CL must be based on a detailed analysis which is the aim of the present work.

In this work, two-reactor designs are studied (compared to designs with a larger number of reactors operating simultaneously) which are switched repeatedly to minimize the investment costs and to simplify process operation (see Figure 1). Previously, a conceptual study was conducted by Heidebrecht *et al.* [19] for the cyclic water-gas shift process, which is similar to RWGS-CL. However, the reaction equilibria, which are crucial for the process were neither considered in that work [19] nor in an optimization study on the same process conducted by Logist *et al.* [20]. In a follow-up work by Heidebrecht and Sundmacher [21], a thermodynamic approach was used for the same process to consider the effects of equilibrium limitations. However, the process kinetics were not considered. In all of the previous studies only fixed bed reactor designs were studied. Thus, a detailed analysis considering the interplay between the reaction kinetics and thermodynamic limitations is still missing for the fixed bed reactor as well as for the fluidized bed reactor. The authors are not aware of comparable studies for the RWGS-CL being published yet. In this work, process simulation is used to analyze the dynamic behavior of the RWGS-CL process for a fixed bed and a fluidized bed reactor configuration. Optimization problems are formulated to maximize the average CO concentration and the OSM utilization. The mutual dependency of the optimization objectives is investigated and the results are discussed within the scope of process design.

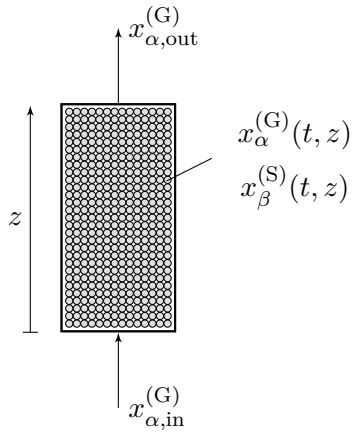

Figure 2: Illustration of a heterogeneous 1D plug flow reactor filled with solid oxygen storage material (OSM).

2. Process Modeling

A fixed bed and a fluidized bed reactor model are developed in the following to study their operational behavior for the RWGS-CL process. In both cases 1D models were chosen as a trade-off between model accuracy and complexity since the transport phenomena in radial direction are expected to be negligible compared to the axial transport.

2.1. Fixed Bed

The RWGS-CL reactor is modeled as a 1D fixed bed reactor filled with solid oxygen storage material (OSM) as depicted in Figure 2. The reactor inlet composition is repeatedly switched between pure CO_2 (oxidation stage) and H_2 (reduction stage), resulting in a cyclic process. Due to the two stages, two different operation modes are possible: co-flow and reverse-flow. Heidebrecht *et al.* showed that application of flow reversal is advantageous [19]. Therefore, reverse-flow operation is used for the fixed bed reactor design, i.e. the gas flows in opposite direction during the reduction and oxidation stage. Isothermal operation is assumed since all reactions have only moderate reaction enthalpies. Sufficient heating and cooling for isothermal operation can be ensured by using multi-tube reactor designs to enlarge the heat transfer area. Thus, the mass balance equations are sufficient to model the reactor. The change of the mole fraction of a gas component α in the gas phase, $x^{(G)}_{\alpha}$, is described by

$$\frac{\partial x^{(G)}_{\alpha}}{\partial t} = -\frac{v^{(G)}}{\varepsilon}\frac{\partial x^{(G)}_{\alpha}}{\partial z} + \frac{(1-\varepsilon)\rho^{(S)}}{\varepsilon c^{(G)}_{t}}\sum_{j}^{N_R}\nu_{\alpha,j}r_j \qquad \forall\alpha = \{\mathrm{H_2},\mathrm{H_2O},\mathrm{CO},\mathrm{CO_2}\}\,, \tag{6}$$

where $v^{(G)}$ is the superficial gas phase velocity, ε the fixed bed void fraction, $\rho^{(S)}$ the density of the solid OSM and $c_t^{(G)}$ the total gas concentration. Chemical reactions are considered by the last term on the right hand side of equation (6), where $[r_j] = \mathrm{mol}/(\mathrm{kg}^{(\mathrm{S})}\mathrm{s})$. The mole fraction of a solid component β in the solid phase is described by

$$\frac{\partial x_\beta^{(S)}}{\partial t} = M^{(S)} \sum_j^{N_R} \nu_{\beta,j} r_j \qquad \forall \beta = \left\{\mathrm{Fe}, \mathrm{FeO}, \mathrm{FeO}_{4/3}\right\}, \tag{7}$$

where $M^{(S)}$ is the molar mass of the solid oxygen storage material, which is approximated as a mean value (see section 2.4). For a detailed derivation of the model equations, the reader is referred to Appendix A.

2.2. Fluidized Bed

The two-region model for bubbling beds with intermediate sized particles from Kunii and Levenspiel is used to model the fluidized bed reactor for RWGS-CL [22] as illustrated in Figure 3. One spatial dimension, z, is considered while gradients in the radial direction are neglected. Gas with the composition $x_{\alpha,\mathrm{in}}^{(\mathrm{G})}$ is entering the reactor with a velocity of $v^{(G)}$ (superficial velocity). Two regions are established in the reactor: the emulsion region (e) and the bubble region (b). The size of the regions is characterized by the bubble fraction δ. In the emulsion region, the solid particles are dispersed in a gas phase that rises with a velocity of $v^{(e)}$, while the bubble region is assumed to only consist of gas which is rises along the reactor at a velocity $v^{(b)}$. Therefore, the bubble region effectively acts as a gas bypass in the reactor. However, gas is exchanged between the emulsion and the bubble region with a rate that depends on the bubble-emulsion gas interchange coefficient $K^{(be)}$. Chemical reactions (r_j^M) are assumed to occur only in the emulsion region. The solid composition is denoted by $x_\beta^{(\mathrm{S})}(t,z)$, while the gas composition in the emulsion and bubble region is denoted by $x_\alpha^{(\mathrm{e})}(t,z)$ and $x_\alpha^{(\mathrm{b})}(t,z)$, respectively. Gas leaves the reactor with the composition $x_{\alpha,\mathrm{out}}^{(\mathrm{G})}$.

The model equations for the two-region fluidized bed model are given in the following:

$$\frac{\partial x_\alpha^{(b)}}{\partial t} = -v^{(b)} \frac{\partial x_\alpha^{(b)}}{\partial z} - K^{(be)}(x_\alpha^{(b)} - x_\alpha^{(e)}) \qquad \forall \alpha = \{\mathrm{H_2}, \mathrm{H_2O}, \mathrm{CO}, \mathrm{CO_2}\} \tag{8}$$

$$\frac{\partial x_\alpha^{(e)}}{\partial t} = -v^{(e)} \frac{\partial x_\alpha^{(e)}}{\partial z} + \frac{\delta}{(1-\delta)\varepsilon_{\mathrm{mf}}} K^{(be)}(x_\alpha^{(b)} - x_\alpha^{(e)}) + \frac{1-\varepsilon_{\mathrm{mf}}}{\varepsilon_{\mathrm{mf}}} \frac{\rho^{(S)}}{c_t^{(G)}} \sum_j^{N_R} \nu_{\alpha,j} r_j^M \quad \forall \alpha = \{\mathrm{H_2}, \mathrm{H_2O}, \mathrm{CO}, \mathrm{CO_2}\} \tag{9}$$

$$\frac{\partial x_\beta^{(S)}}{\partial t} = D_v^{(S)} \frac{\partial^2 x_\beta^{(S)}}{\partial z^2} + M^{(S)} \sum_j^{N_R} \nu_{\beta,j} r_j^M \qquad \forall \beta = \left\{\mathrm{Fe}, \mathrm{FeO}, \mathrm{FeO}_{4/3}\right\} \tag{10}$$

For a detailed derivation of the model equations, the reader is referred to Appendix B.

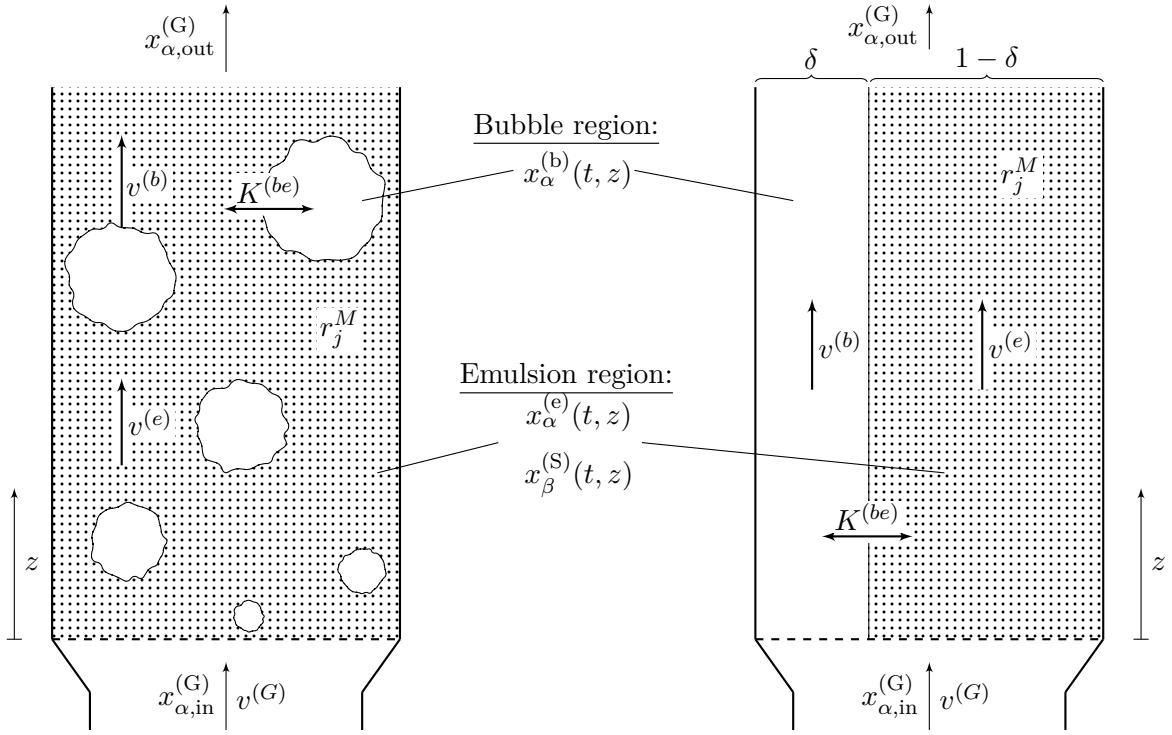

Figure 3: Left: illustration of a 1D two-region, heterogeneous fluidized bed reactor with solid oxygen storage material (OSM). Right: schematic representation for modeling.

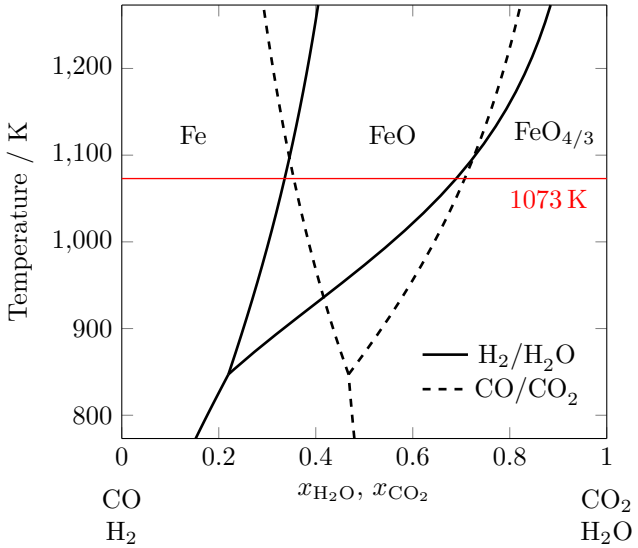

Figure 4: Baur-Glaessner diagram showing the equilibrium between the oxidation states of iron with regard to the gas composition of H_2/H_2O (solid lines) and CO/CO_2 (dashed lines) mixtures. For temperatures below 847 K FeO is not stable.

2.3. Kinetics

The oxidation and reduction stage each proceed in two consecutive reaction steps through the intermediate product FeO according to equations (2) to (5). All reactions are strongly equilibrium limited. The Baur-Glaessner diagram [23] in Figure 4 shows the phase equilibria for iron in its different oxidation states with gas mixtures of H_2/H_2O and CO/CO_2. The solid and dashed lines delineate the phase equilibria between the three solid phases Fe, FeO and $FeO_{4/3}$ (FeO is only stable at $T > 847\,\mathrm{K}$) with regard to the gas composition. To completely reduce $FeO_{4/3}$ to Fe at 1073 K, the hydrogen mole fraction of the surrounding gas must be $x_{H_2} > 0.66$. Similarly, for complete oxidation of Fe to $FeO_{4/3}$ at 1073 K, the CO_2 mole fraction must be $x_{CO_2} > 0.70$. Furthermore, it can be seen that the oxidation and reduction each proceed in two consecutive steps with a distinct equilibrium gas composition according to equations (2) to (5). The reaction rate expressions are formulated to account for the equilibrium limitations of the reactions (equations (11) to (14)). They are based on a previous study on the water-gas shift chemical looping process of Hertel *et al.* [24]. Unlike conventional equilibrium reaction rate expressions for equilibrium limited gas phase reactions, the rates are piecewise defined because the forward and backward rates depend not only on the gas composition but also on the solid oxidation state. The importance of using different reaction rate expressions for the forward and backward direction of equilibrium limited gas-solid reactions was highlighted by Sohn [25].

$$r_1^M = \begin{cases} k_O^0 \cdot \exp\left(\frac{-E_{A,O}}{RT}\right) \cdot \left(x_{\mathrm{Fe}}^{(S)}\right)^{n_O} \cdot Y_{\mathrm{C}} \left(y_{\mathrm{CO_2}}^{(G)} - \frac{y_{\mathrm{CO}}^{(G)}}{K_{\mathrm{eq},1}}\right)^{m_O}, & \text{if } \frac{y_{\mathrm{CO}}^{(G)}}{y_{\mathrm{CO_2}}^{(G)}} < K_{\mathrm{eq},1} \\ -k_O^0 \cdot \exp\left(\frac{-E_{A,O}}{RT}\right) \cdot \left(x_{\mathrm{FeO}}^{(S)}\right)^{n_O} \cdot Y_{\mathrm{C}} \left(\frac{y_{\mathrm{CO}}^{(G)}}{K_{\mathrm{eq},1}} - y_{\mathrm{CO_2}}^{(G)}\right)^{m_O}, & \text{if } \frac{y_{\mathrm{CO}}^{(G)}}{y_{\mathrm{CO_2}}^{(G)}} > K_{\mathrm{eq},1} \end{cases} \tag{11}$$

$$r_2^M = \begin{cases} k_O^0 \cdot \exp\left(\frac{-E_{A,O}}{RT}\right) \cdot \left(x_{\mathrm{FeO}}^{(S)}\right)^{n_O} \cdot Y_{\mathrm{C}} \left(y_{\mathrm{CO_2}}^{(G)} - \frac{y_{\mathrm{CO}}^{(G)}}{K_{\mathrm{eq},2}}\right)^{m_O}, & \text{if } \frac{y_{\mathrm{CO}}^{(G)}}{y_{\mathrm{CO_2}}^{(G)}} < K_{\mathrm{eq},2} \\ -k_O^0 \cdot \exp\left(\frac{-E_{A,O}}{RT}\right) \cdot \left(x_{\mathrm{FeO_{4/3}}}^{(S)}\right)^{n_O} \cdot Y_{\mathrm{C}} \left(\frac{y_{\mathrm{CO}}^{(G)}}{K_{\mathrm{eq},2}} - y_{\mathrm{CO_2}}^{(G)}\right)^{m_O}, & \text{if } \frac{y_{\mathrm{CO}}^{(G)}}{y_{\mathrm{CO_2}}^{(G)}} > K_{\mathrm{eq},2} \end{cases} \tag{12}$$

$$r_3^M = \begin{cases} k_R^0 \cdot \exp\left(\frac{-E_{A,R}}{RT}\right) \cdot \left(x_{\mathrm{FeO_{4/3}}}^{(S)}\right)^{n_R} \cdot Y_{\mathrm{H}} \left(y_{\mathrm{H_2}}^{(G)} - \frac{y_{\mathrm{H_2O}}^{(G)}}{K_{\mathrm{eq},3}}\right)^{m_R}, & \text{if } \frac{y_{\mathrm{H_2O}}^{(G)}}{y_{\mathrm{H_2}}^{(G)}} < K_{\mathrm{eq},3} \\ -k_R^0 \cdot \exp\left(\frac{-E_{A,R}}{RT}\right) \cdot \left(x_{\mathrm{FeO}}^{(S)}\right)^{n_R} \cdot Y_{\mathrm{H}} \left(\frac{y_{\mathrm{H_2O}}^{(G)}}{K_{\mathrm{eq},3}} - y_{\mathrm{H_2}}^{(G)}\right)^{m_R}, & \text{if } \frac{y_{\mathrm{H_2O}}^{(G)}}{y_{\mathrm{H_2}}^{(G)}} > K_{\mathrm{eq},3} \end{cases} \tag{13}$$

$$r_4^M = \begin{cases} k_R^0 \cdot \exp\left(\frac{-E_{A,R}}{RT}\right) \cdot \left(x_{\mathrm{FeO}}^{(S)}\right)^{n_R} \cdot Y_{\mathrm{H}} \left(y_{\mathrm{H_2}}^{(G)} - \frac{y_{\mathrm{H_2O}}^{(G)}}{K_{\mathrm{eq},4}}\right)^{m_R}, & \text{if } \frac{y_{\mathrm{H_2O}}^{(G)}}{y_{\mathrm{H_2}}^{(G)}} < K_{\mathrm{eq},4} \\ -k_R^0 \cdot \exp\left(\frac{-E_{A,R}}{RT}\right) \cdot \left(x_{\mathrm{Fe}}^{(S)}\right)^{n_R} \cdot Y_{\mathrm{H}} \left(\frac{y_{\mathrm{H_2O}}^{(G)}}{K_{\mathrm{eq},4}} - y_{\mathrm{H_2}}^{(G)}\right)^{m_R}, & \text{if } \frac{y_{\mathrm{H_2O}}^{(G)}}{y_{\mathrm{H_2}}^{(G)}} > K_{\mathrm{eq},4} \end{cases} \tag{14}$$

Here, k^0, E_A, n and m are kinetic constants for the oxidation (index O) and reduction (index R) reactions. The direction of the reaction depends on the current gas phase composition and the chemical equilibrium constant $K_{\mathrm{eq},i}$ of reaction i. Furthermore, y_i denotes the ratio of the mole fractions of CO/CO_2 and H_2/H_2O.

Table 1: Kinetic parameters for the oxidation and reduction reactions from Wenzel *et al.* [3].

Parameter	Oxidation	Reduction
n	1.002	0.724
m	0.618	0.461
k^0 / mol/kg$_{\mathrm{OSM}}$/s	18199	1140
E_A / kJ/mol	111.6	80.7

They are defined as follows:

$$y_{\mathrm{CO}}^{(G)} = \frac{x_{\mathrm{CO}}^{(G)}}{x_{\mathrm{CO}}^{(G)} + x_{\mathrm{CO_2}}^{(G)}} \tag{15}$$

$$y_{\mathrm{CO_2}}^{(G)} = \frac{x_{\mathrm{CO_2}}^{(G)}}{x_{\mathrm{CO}}^{(G)} + x_{\mathrm{CO_2}}^{(G)}} \tag{16}$$

$$y_{\mathrm{H_2}}^{(G)} = \frac{x_{\mathrm{H_2}}^{(G)}}{x_{\mathrm{H_2}}^{(G)} + x_{\mathrm{H_2O}}^{(G)}} \tag{17}$$

$$y_{\mathrm{H_2O}}^{(G)} = \frac{x_{\mathrm{H_2O}}^{(G)}}{x_{\mathrm{H_2}}^{(G)} + x_{\mathrm{H_2O}}^{(G)}} \tag{18}$$

The carbon and hydrogen content is defined by Y_C and Y_H, respectively:

$$Y_C = x_{\mathrm{CO}}^{(G)} + x_{\mathrm{CO_2}}^{(G)} \tag{19}$$

$$Y_H = x_{\mathrm{H_2}}^{(G)} + x_{\mathrm{H_2O}}^{(G)} \tag{20}$$

The necessary parameters for the kinetics are taken from Wenzel *et al.* [3] and are summarized in Table 1. A detailed derivation of the reaction rate expressions can be found in Appendix C.

2.4. Model Parameters and Fluid Dynamics

A reactor length of $L = 2\,\mathrm{m}$ is chosen being a small scale industrial fixed bed reactor. The effectiveness factor of the RWGS reaction on Ni-catalyst particles with a mean diameter of 3 mm was estimated by Wolf *et al.* to be $\eta_{\mathrm{eff}} = 0.1$ [26]. Hertel *et al.* found a value of $\eta_{\mathrm{eff}} = 0.3$ for iron oxide particles with a mean diameter of 3 mm [24]. Therefore, a mean value for the effectiveness factor of $\eta_{\mathrm{eff}} = 0.2$ was chosen. For the solid, a mean density of $\rho^{(S)} = 6000\,\mathrm{kg/m^3}$ [27] and a mean molar mass of $M^{(S)} = 67\,\mathrm{g/mol}$ are assumed. The fixed bed void fraction is set to $\varepsilon = 0.5$, according to Hertel *et al.* [24]. Both reactor configurations are operated at $T = 1073\,\mathrm{K}$ and $p = 1\,\mathrm{atm}$. Temperature is fixed in all cases. From a theoretical perspective the temperature should be as high as possible to shift the reaction equilibrium to the product side (since all reactions except for one are endothermic) and to accelerate the reaction kinetics. However, from a practical point of view high temperature leads to material stability problems and it has been shown in our

previous work that 1073 K is the highest permissible temperature for 80 wt% Fe_2O_3 to allow for repeated cycling without too severe material degradation [3]. Different temperatures during oxidation and reduction were not permitted in this study because it has been mentioned numerous times in the literature that the necessary heat recuperation between the two steps in non-isothermal operation is severely decreasing the energy efficiency [28]. Therefore, isothermal operation is preferred for chemical looping processes. Standard pressure is chosen since the used kinetic parameters (see Table 1) were determined at that pressure. Since all reactions are equimolar there is no pressure dependence of the equilibrium composition. The total gas concentration $c_t^{(G)}$ is calculated using the ideal gas law. For the calculation of the chemical equilibrium constants, K_{eq}, thermodynamic data from CRC Handbook and Yaws were used [29, 27].

The flow field in the fluidized bed is not solved explicitly *via* the momentum balance but semi-empirical relationships are used to characterize the fluid dynamic behavior of the reactor. This is a typical approach for fluidized bed reactor modeling and yields a reasonable compromise between model simplicity and level of detail. The relationships used in this study are based on the model by Kunii and Levenspiel for intermediate sized particles [22]. The mean particle size for the oxygen storage material is $d_p = 250\,\mu\mathrm{m}$ (Geldart Type B [30]). A fluidized bed reactor is assumed with an inner diameter of $d_t = 0.8\,\mathrm{m}$ and a bed height of $L = 2\,\mathrm{m}$ at fluidization conditions to be comparable in size to the fixed bed reactor. The minimum fluidization voidage is approximated to be $\varepsilon_{\mathrm{mf}} = 0.55$, according to Kunii and Levenspiel [31]. Thus, the total amount of OSM inside the reactor is $2059.1\,\mathrm{kg_{OSM}}$ (for the fixed bed reactor to hold the same amount of OSM the reactor diameter must be $d_t = 0.661\,\mathrm{m}$). The minimum fluidization velocity v_{mf} can be calculated according to eq. (21) [31]:

$$v_{\mathrm{mf}} = \frac{\mu}{d_p \rho^{(G)}} \left(\sqrt{28.7^2 + 0.0494 \left(\frac{d_p^3 \rho^{(G)} (\rho^{(S)} - \rho^{(G)}) g}{\mu^2} \right)} - 28.7 \right) \tag{21}$$

Here, the gas phase density and the dynamic viscosity are denoted by $\rho^{(G)}$ and μ, respectively. Mean values of all gas components are used as an approximation since the actual gas composition changes along the reactor. Thus, at a temperature of 1073 K the gas phase density and the dynamic viscosity are $\rho^{(G)} = 0.261\,\mathrm{kg/m^3}$ and $\mu = 3.66 \times 10^{-5}\,\mathrm{Pas}$, respectively. The ideal gas law is used for calculating the gas density. The dynamic viscosity is calculated by a correlation from VDI Wärmeatlas [32]. The correlation is only valid for $T < 773\,\mathrm{K}$ but since there are no values available for the gas viscosity at the process temperature, this correlation is extrapolated. We assume that the values give a reasonable approximation of the true viscosity. The emulsion phase velocity $v^{(e)}$ is calculated by eq. (22).

$$v^{(e)} = \frac{2}{3} v_{\mathrm{mf}} + \frac{1}{3} v^{(G)} \tag{22}$$

Here, $v^{(G)}$ is the superficial inlet velocity into the reactor, which is assumed to be 0.6 m/s in both reaction stages (this corresponds to a bubbling fluidized bed regime according to Kunii and Levenspiel [31]). For the calculation of the bubble phase velocity $v^{(b)}$, the bubble diameter has to be known first. From eq. (23), the bubble diameter at height z can be estimated.

$$d_b = d_{bm} - (d_{bm} - d_{b0}) \exp(-0.3z/d_t) \tag{23}$$

The initial bubble size d_{b0} and the limiting bubble size d_{bm} can be estimated by the following equations:

$$d_{b0} = \frac{2.78}{g}(v^{(G)} - v_{\mathrm{mf}})^2 \tag{24}$$

$$d_{bm} = 0.65 \left[\frac{\pi}{4} d_t^2 (v^{(G)} - v_{\mathrm{mf}})\right]^{0.4}, \qquad [\mathrm{m}] \tag{25}$$

Thus, at height $z = 1$ m the bubble size is estimated to be $d_b = 0.1$ m. The bubble rise velocity v_{br} for single bubbles is given by eq. (26).

$$v_{br} = 0.711(g d_b)^{1/2} \tag{26}$$

With v_{br}, the bubble gas velocity can be estimated by eq. (27).

$$v^{(b')} = v^{(G)} - v_{\mathrm{mf}} + v_{br} \tag{27}$$

For the model, the rise velocity of bubble gas

$$v^{(b)} = v^{(b')} + 3v_{\mathrm{mf}} \tag{28}$$

is used instead of the bubble gas velocity $v^{(b')}$. The gas interchange coefficient between bubble and emulsion phase $K^{(be)}$ can be estimated from the minimum fluidization velocity and the particle diameter by eq. (29).

$$K^{(be)} = 4.5 \left(\frac{v_{\mathrm{mf}}}{d_b}\right) \tag{29}$$

The average vertical dispersion coefficient of the solids $D_v^{(S)}$ is estimated by eq. (30).

$$D_v^{(S)} = 0.3 d_t^{0.65}, \qquad [\mathrm{m}^2/\mathrm{s}] \tag{30}$$

The bubble fraction δ is calculated according to the following equation.

$$\delta = \frac{v_0 - v_{mf}}{v_b} \tag{31}$$

2.5. Optimization

An important value for process characterization is the degree of reduction of the oxygen storage material, denoted by α. By definition, $\alpha = 1$ for $x_{\mathrm{Fe}}^{(S)} = 1$ and $\alpha = 0$ for $x_{\mathrm{FeO_{4/3}}}^{(S)} = 1$. For $x_{\mathrm{FeO}}^{(S)} = 1$, 25 % of the available oxygen is released, i.e. $\alpha = 0.25$. Thus, the degree of reduction can be calculated from the solid mole fractions according to

$$\alpha(t, z) = x_{\mathrm{Fe}}^{(S)}(t, z) + 0.25 x_{\mathrm{FeO}}^{(S)}(t, z). \tag{32}$$

Due to the cyclic nature of the RWGS-CL process at least two reactors are needed for continuous production of syngas. Fernández and Abanades designed a continuous chemical looping combustion (CLC) system consisting of eight reactors [33]. In a similar study by Spallina *et al.* 16 reactors were reported [34]. However, in CLC more process steps are involved (heat removal, purging) which are not necessary for RWGS-CL. Thus, intelligent design and optimized process parameters may lead to a minimum number of reactors. For the following optimization problem, a fixed number of two reactors is assumed to simplify the process design and operation.

The duration of the oxidation and the reduction phase are denoted as t_{Ox} and t_{Red}, respectively, and are optimized for the fixed and fluidized bed reactor design. The most important criterion for continuous production of syngas is that the duration of the reduction phase (regeneration of the reactor) is shorter than the oxidation phase (production of CO), i.e. $t_{\mathrm{Red}} < t_{\mathrm{Ox}}$ assuming that switching of the gas streams occurs instantly. To change the duration of the two phases, the gas flow velocities $v_{\mathrm{in,Ox}}^{(G)}$ and $v_{\mathrm{in,Red}}^{(G)}$ were adjusted as well. However, higher gas flows and shorter reaction times lead to incomplete OSM utilization in the reactor and/or decreased gas conversion. Furthermore, the gas flow velocities can only be adjusted in the fixed bed reactor design. For fluidized bed operation, the gas inlet velocities must be fixed to yield defined flow characteristics.

To analyze process operation, two performance indicators were defined in this study. The first indicator is the OSM utilization which is quantified by the difference of the spatial mean value of the reduction extent ($\bar{\alpha}$) at the end of each reaction phase. In the reduction stage, the reduction extent should approach one to ensure the highest OSM utilization. Equivalently, in the oxidation stage, the reduction extent preferably approaches zero. The OSM utilization, denoted by X_{OSM}, is defined by the following term:

$$X_{\mathrm{OSM}} = \bar{\alpha}_{\mathrm{Red}}(t = t_{\mathrm{Red}}) - \bar{\alpha}_{\mathrm{Ox}}(t = t_{\mathrm{Ox}}) \tag{33}$$

Thus, complete reduction of the OSM after the reduction stage and complete oxidation of the OSM after the oxidation stage yields an OSM utilization of $X_{\mathrm{OSM}} = 1$. High values for X_{OSM} lead to reduced reactor size and costs as the OSM is used more effectively.
The second performance indicator is the average CO concentration in the outlet gas of during the oxidation stage which is defined by the following term,

$$\bar{x}_{\mathrm{CO}} = \frac{\int_0^{t_{\mathrm{Ox}}} x^{(G)}_{\mathrm{CO,out}}(t)\mathrm{d}t}{t_{\mathrm{Ox}}} \tag{34}$$

where $x^{(G)}_{\mathrm{CO,out}}(t)$ is the mole fraction of CO at the reactor outlet during the oxidation phase. High average CO concentrations are preferable for downstream product purification. Both performance indicators are important for efficient process operation. However, the two indicators are competing and a trade-off solution must be found between these two values for both reactor designs. To further ensure feasible and efficient operation, additional constraints are introduced in the following. The use of hydrogen in the reduction stage should be minimized, since its sustainable production is the most energy consuming step in the production of syngas *via* RWGS-CL [1]. Thus, we define that the mole fraction of H_2 in the outlet stream during the reduction stage should not exceed a value of $x^{(G)}_{\mathrm{H_2,out}} = 0.99$. This ensures a reasonable H_2 conversion in the reduction stage and excessive H_2 slip is minimized. Furthermore, a minimum outlet CO concentration should be ensured during the oxidation phase to allow for efficient downstream purification. Downstream gas purification typically prefers a steady gas composition. In this study, the value for the minimum outlet CO concentration was set to $x^{(G)}_{\mathrm{CO,out}} = 0.1$.

Optimization problems are formulated in the following for maximizing the previously defined performance indicators under the mentioned operation constraints.

2.5.1. Fixed Bed Reactor

Maximizing the OSM utilization X_{OSM}:

$$\begin{aligned} \max_{t_{\mathrm{Red}}, t_{\mathrm{Ox}}, v^{(G)}_{\mathrm{Red}}, v^{(G)}_{\mathrm{Ox}}} \quad & X_{\mathrm{OSM}} \\ \text{s.t.} \quad & \text{Fixed bed model equations} \\ & t_{\mathrm{Red}} \leq t_{\mathrm{Ox}} \\ & x^{(G)}_{\mathrm{H_2,out}}(t) \leq 0.99 \\ & x^{(G)}_{\mathrm{CO,out}}(t) \geq 0.1 \end{aligned} \tag{35}$$

The decision variables for optimization of the fixed bed reactor are the period times t_{Red} and t_{Ox} as well as the gas inlet velocities $v^{(G)}_{\mathrm{Red}}$ and $v^{(G)}_{\mathrm{Ox}}$ for the reduction and the oxidation stage, respectively.

Maximizing the average CO concentration $\bar{x}_{\mathrm{CO}}$ at the reactor outlet during the oxidation stage:

$$\begin{aligned} \max_{t_{\mathrm{Red}}, t_{\mathrm{Ox}}, v_{\mathrm{Red}}^{(G)}, v_{\mathrm{Ox}}^{(G)}} \quad & \bar{x}_{\mathrm{CO}} \\ \text{s.t.} \quad & \text{Fixed bed model equations} \\ & t_{\mathrm{Red}} \leq t_{\mathrm{Ox}} \\ & x_{\mathrm{H_2,out}}^{(G)}(t) \leq 0.99 \\ & x_{\mathrm{CO,out}}^{(G)}(t) \geq 0.1 \end{aligned} \tag{36}$$

2.5.2. Fluidized Bed Reactor

Maximizing the OSM utilization X_{OSM}:

$$\begin{aligned} \max_{t_{\mathrm{Red}}, t_{\mathrm{Ox}}} \quad & X_{\mathrm{OSM}} \\ \text{s.t.} \quad & \text{Fluidized bed model equations} \\ & t_{\mathrm{Red}} \leq t_{\mathrm{Ox}} \\ & x_{\mathrm{H_2,out}}^{(G)}(t) \leq 0.99 \\ & x_{\mathrm{CO,out}}^{(G)}(t) \geq 0.1 \end{aligned} \tag{37}$$

For the fluidized bed reactor, the decision variables are only the period times t_{Red} and t_{Ox} for the reduction and the oxidation stage, respectively.

Maximizing the average CO concentration $\bar{x}_{\mathrm{CO}}$ at the reactor outlet during the oxidation stage:

$$\begin{aligned} \max_{t_{\mathrm{Red}}, t_{\mathrm{Ox}}} \quad & \bar{x}_{\mathrm{CO}} \\ \text{s.t.} \quad & \text{Fluidized bed model equations} \\ & t_{\mathrm{Red}} \leq t_{\mathrm{Ox}} \\ & x_{\mathrm{H_2,out}}^{(G)}(t) \leq 0.99 \\ & x_{\mathrm{CO,out}}^{(G)}(t) \geq 0.1 \end{aligned} \tag{38}$$

2.6. Solution Strategy

The model equations of the fixed and fluidized bed reactor designs are discretized with the finite volume method (FVM). The resulting system of ordinary differential equations (ODEs) is solved with the *ode15s* solver in MATLAB. Discretization and subsequent solution of the ODE system was found to be faster than a full discretization approach by Munera Parra *et al.* for a similar problem [35]. The piecewise defined equations for the reaction rates resulted numerical difficulties when using implicit solvers like *ode15s* in MATLAB. Thus, relaxation techniques were used to approximate the piecewise defined functions by differentiable functions (see Appendix C). To assess the real process performance, the process has to be simulated several times until the cyclic steady-state (CSS) is reached. The CSS solution is obtained by successive substitution, i.e. the end state of one simulation is used for the initial values for the next

simulation until the CSS is reached. The criterion for CSS is defined as

$$\sum_{z=0}^{L}\left(x_{\mathrm{new}}^{(S)}(t_{\mathrm{Red}},z)-x_{\mathrm{old}}^{(S)}(t_{\mathrm{Red}},z)\right)^2+\sum_{z=0}^{L}\left(x_{\mathrm{new}}^{(S)}(t_{\mathrm{Ox}},z)-x_{\mathrm{old}}^{(S)}(t_{\mathrm{Ox}},z)\right)^2<1\times10^{-3}$$

Here, $x_{\mathrm{new}}^{(S)}$ and $x_{\mathrm{old}}^{(S)}$ denote the solid composition at the respective period time of the reduction and oxidation phase, t_{Red} and t_{Ox}. Thus, CSS is reached when the sum of squared errors between the solids composition of the new and the old simulation run is be below 1×10^{-3}. Depending on the operating parameters, up to 50 simulation runs have to be computed to reach CSS. The optimization problem is superimposed on top of the simulation and was solved with MATLAB's *fminsearch* function, where the optimization constraints were formulated as penalty terms in the objective function. In each iteration step of the optimization, the process has to be simulated until CSS is reached.

3. Results and Discussion

The piecewise defined kinetic expressions coupled with the inherently dynamic behavior of the RWGS-CL process give rise to complex phenomena which are analyzed and discussed in the following. All the results given correspond to the cyclic steady state condition.

3.1. Simulation

Process simulation is used prior to optimization to analyze and understand the general process characteristics and behaviour. Therefore, the optimization constraints discussed in section 2.5 are not applied yet. Two different reaction regimes can be established in the process: an equilibrium limited reaction regime and a rate limited reaction regime. The first case is characterized by low gas velocity (long residence time). Therefore, the gas entering the reactor reacts with the solid and reaches chemical equilibrium almost instantly. Conversely, the rate limited reaction regime is characterized by high gas velocity (short residence time). The reaction kinetics dominate the process dynamics and the gas only reacts to a certain extent, i.e. chemical equilibrium is not reached inside of the reactor. In Figure 5, the simulation results for the equilibrium limited reaction regime are depicted for the fixed bed reactor. In Figure 5a the change of the reaction extent of the OSM throughout the reactor is depicted over time. During reduction, two distinct reaction fronts can be identified, one from Fe to FeO and another from FeO to $FeO_{4/3}$. This leads to two composition changes in the gas outlet as can be seen in Figure 5b. However, during oxidation the two reaction fronts are overlapping and merge into one reaction front. Consequently, the gas outlet only shows one composition change. Heidebrecht *et al.* conducted a wave analysis for a cyclic water-gas shift reactor to study the behavior of reaction fronts [21]. It was shown that the reaction front velocities depend mainly on the chemical equilibria and the stoichiometry of the reactions. Under the conditions investigated in this work, the two reaction fronts in the reduction stage have different velocities. This is due to two reasons: 1)

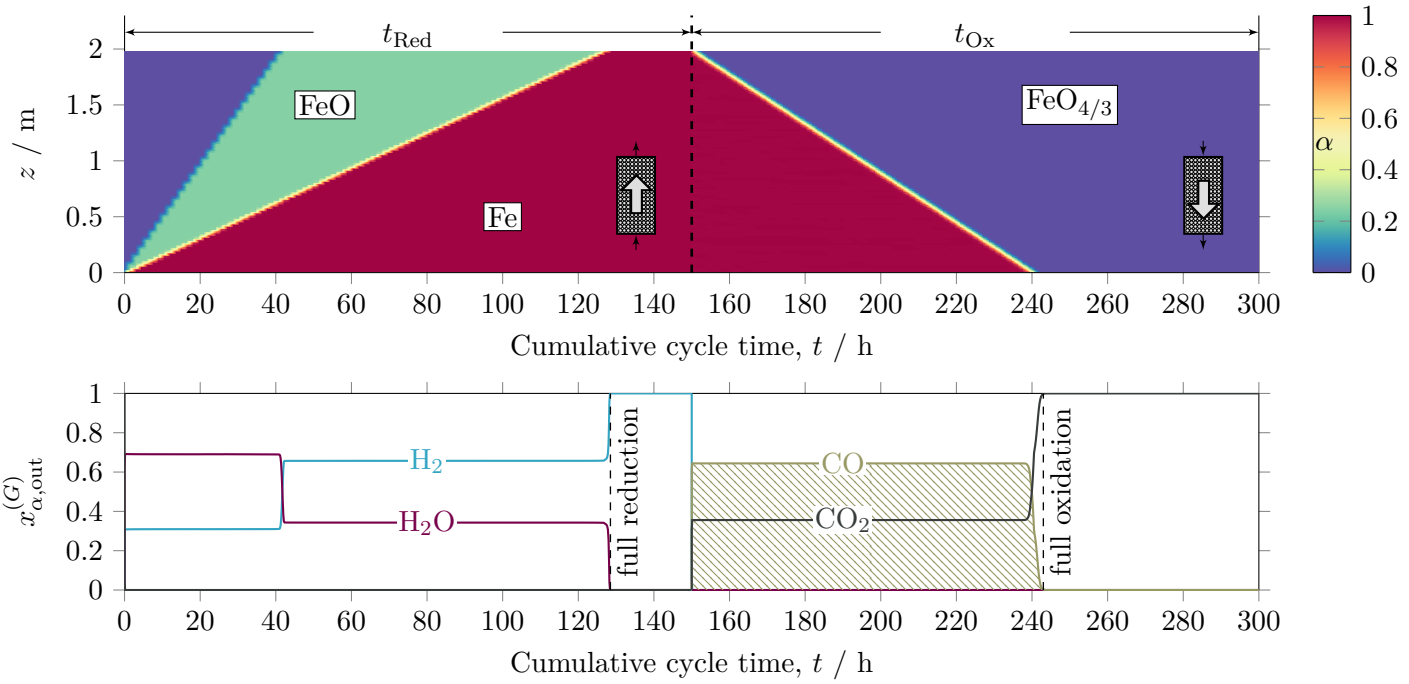

Figure 5: Simulation results for the fixed bed reactor design with $v^{(G)}_{\mathrm{Red}} = v^{(G)}_{\mathrm{Ox}} = 0.05\,\mathrm{m/s}$ and $t_{\mathrm{Red}} = t_{\mathrm{Ox}} = 150\,\mathrm{h}$ (equilibrium limited reaction regime). Reduction extent α as a function of time and axial coordinate z (top) and gas outlet concentration $x^{(G)}_{\alpha,\mathrm{out}}$ as a function of time (bottom). Complete reduction and oxidation achieved after 128.5 h and 93 h, respectively ($X_{\mathrm{OSM}} = 100\%$). Inset indicates the gas flow direction in each stage (reverse-flow).

the equilibrium composition of second reaction step from FeO to Fe is on the reactant side, i.e. $K_{\mathrm{eq}} < 1$ (see Figure 4) and 1 mol oxygen must be exchanged between the gas and the solid phase (compared to 1/3 mol oxygen in the first reaction step). The combination of these two factors leads to a low reaction front velocity. The second reaction step is limiting and the two reaction fronts separate during reduction. Conversely, during oxidation the first reaction step from Fe to FeO is limiting and therefore the two reaction fronts are moving with the same velocity. Notice that complete reduction is achieved after about 128.5 h while the material is completely oxidized after 93 h already. Thus, continuous process operation with an OSM utilization of 100% is not possible in this reaction regime when only two reactors are considered because the regeneration stage (reduction) must be faster than the production stage (oxidation).

Figure 6 shows the simulation results for the rate limited reaction regime, i.e. high gas velocities and short residence time. Neither for the reduction nor the oxidation stage clear reaction fronts can be identified now compared to the equilibrium limited reaction regime. Instead, both reaction steps occur simultaneously and the material is gradually reduced and oxidized. The high gas velocities in both stages lead to period times much shorter than under equilibrium limited reaction conditions. However, due to the short residence time chemical equilibrium is not reached inside of the reactor and the gas conversion decreases. This leads

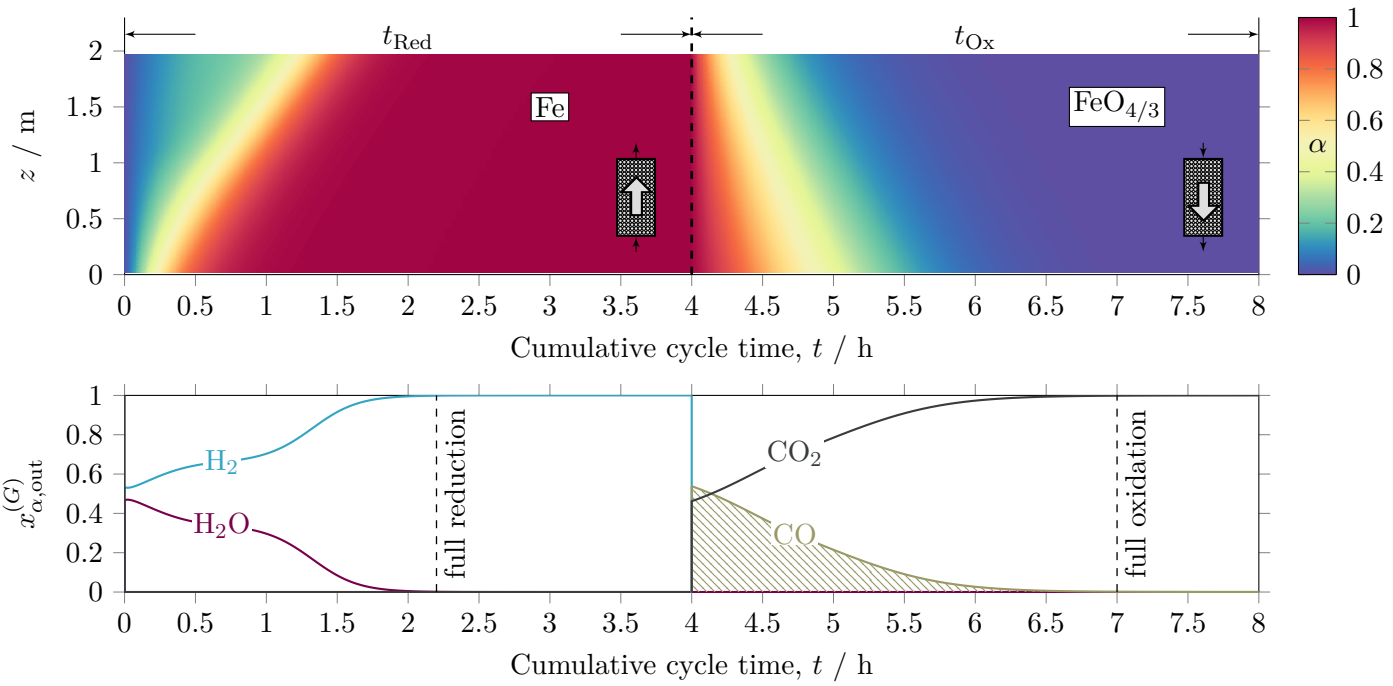

Figure 6: Simulation results for the fixed bed reactor design with $v^{(G)}_{\mathrm{Red}} = v^{(G)}_{\mathrm{Ox}} = 6\,\mathrm{m/s}$ and $t_{\mathrm{Red}} = t_{\mathrm{Ox}} = 4\,\mathrm{h}$ (rate limited reaction regime). Reduction extent α as a function of time and axial coordinate z (top) and gas outlet concentration $x^{(G)}_{\alpha,\mathrm{out}}$ as a function of time (bottom). Complete reduction and oxidation achieved after $\approx 2.2\,\mathrm{h}$ and $\approx 3\,\mathrm{h}$, respectively ($X_{\mathrm{OSM}} = 100\%$). Inset indicates the gas flow direction in each stage (reverse-flow).

to a gradually decreasing CO concentration in the gas outlet and a low average CO concentration during the oxidation stage. Furthermore, the low conversion of H_2 during the reduction stage leads to a higher overall energy demand as H_2 production is the most energy consuming part of the overall process [1]. However, the unreacted H_2 can be separated and recycled easily by condensing the water in the outlet stream during reduction. An important difference compared to the equilibrium limited case is that complete reduction is achieved in less time ($\approx 2.2\,\mathrm{h}$) than complete oxidation ($\approx 3\,\mathrm{h}$). Consequently, in the rate limited reaction regime a continuous process operation with an OSM utilization of 100% is possible with only two reactors. It can be concluded that the overall process behavior is strongly dependent on the selected gas inlet velocities.

For the fluidized bed reactor design, the gas flow velocities are fixed to $v^{(G)}_{\mathrm{Red}} = v^{(G)}_{\mathrm{Ox}} = 0.6\,\mathrm{m/s}$ to yield a bubbling fluidized bed behavior. Therefore, only one case was studied here in contrast to the fixed bed reactor design. Figure 7 shows the solid composition as a function of time (under the investigated conditions the solids are perfectly mixed, i.e. there is no spatial gradient along z). In both stages, the reaction steps proceed consecutively, i.e. the second reaction step starts only after completion of the first reaction step. This is due to the perfect mixing of the OSM inside the reactor. Furthermore, the gas entering the reactor is in chemical equilibrium almost instantly (see equilibrium limited reaction regime in the fixed bed case).

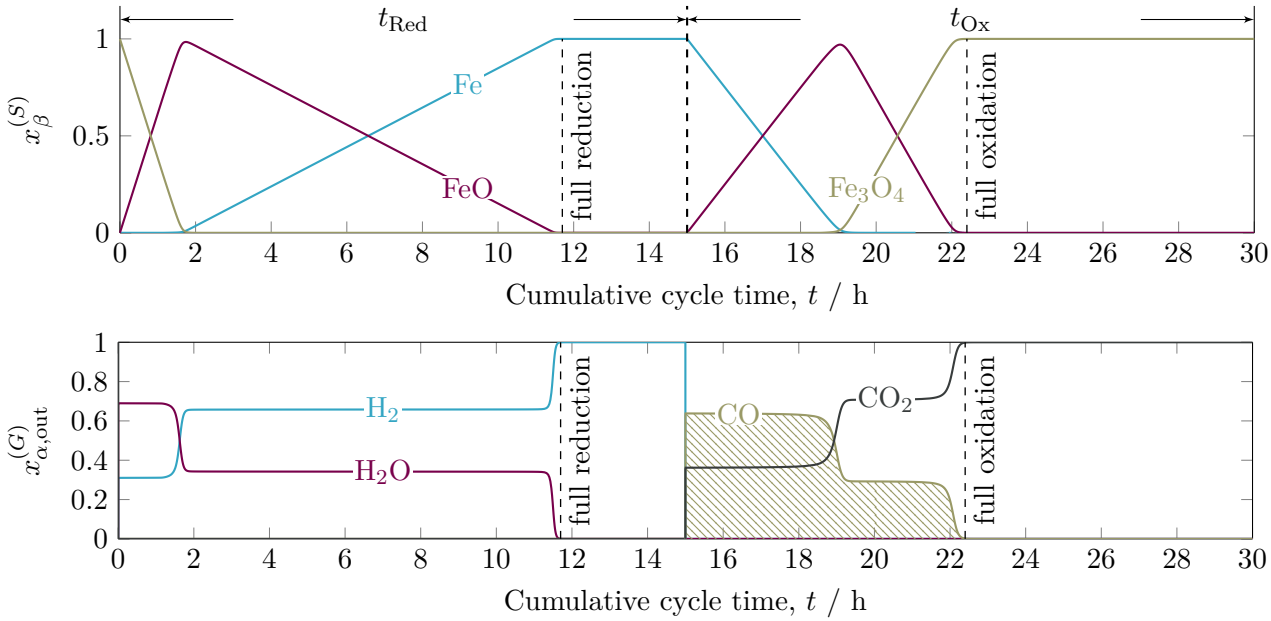

Figure 7: Simulation results for the fluidized bed reactor design with $v_{\mathrm{Red}}^{(G)} = v_{\mathrm{Ox}}^{(G)} = 0.6\,\mathrm{m/s}$ and $t_{\mathrm{Red}} = t_{\mathrm{Ox}} = 15\,\mathrm{h}$. Reduction extent α as a function of time and axial coordinate z (top) and gas outlet concentration $x_{\alpha,\mathrm{out}}^{(G)}$ as a function of time (bottom). Complete reduction and oxidation achieved after 11.6 h and 7.3 h, respectively ($X_{\mathrm{OSM}} = 100\%$).

In the beginning of the reduction stage, the H_2 outlet concentration is $x_{H_2}^{(G)} = 0.31$ (corresponding to the equilibrium concentration of the first reaction step from $FeO_{4/3}$ to FeO). However, as mentioned in section 2.3, for reduction of FeO to Fe the H_2 concentration must be at least $x_{H_2}^{(G)} = 0.66$. Thus, the reaction from FeO to Fe will not proceed since the reduction potential of the gas is too low. The two reactions from Fe to FeO and from FeO to $FeO_{4/3}$ in the oxidation stage proceed in consecutively for the same reason. This leads to two distinct concentration fronts in the gas outlet during oxidation and reduction. Similarly to the fixed bed reactor design with low gas velocities, the reduction is shorter than the oxidation, i.e. complete reduction is achieved after 11.7 h while complete oxidation is achieved already after 7.4 h. Therefore, with the fluidized bed reactor configuration a continuous process operation with an OSM utilization of 100% is not achievable when only two reactors are considered.

3.2. Optimization

Both reactor designs were optimized with regard to the average CO concentration and the OSM utilization as defined in section 2.5. The results for maximizing the OSM utilization for the fixed bed reactor design (see equation (35)) are shown in Figure 8. A period time ($t_{\mathrm{Red}} = 3.53\,\mathrm{h}$) and a gas velocity ($v_{\mathrm{Red}}^{(G)} = 2.04\,\mathrm{m/s}$) are optimal for reduction. Thus, the reduction stage is shorter than the oxidation stage as specified by the constraints to enable quasi-continuous operation with only two reactors. The period time of the oxidation stage is longer ($t_{\mathrm{Ox}} = 4.90\,\mathrm{h}$) and a low gas velocity ($v_{\mathrm{Ox}}^{(G)} = 1.07\,\mathrm{m/s}$) is optimal. Thus, the reactor conditions

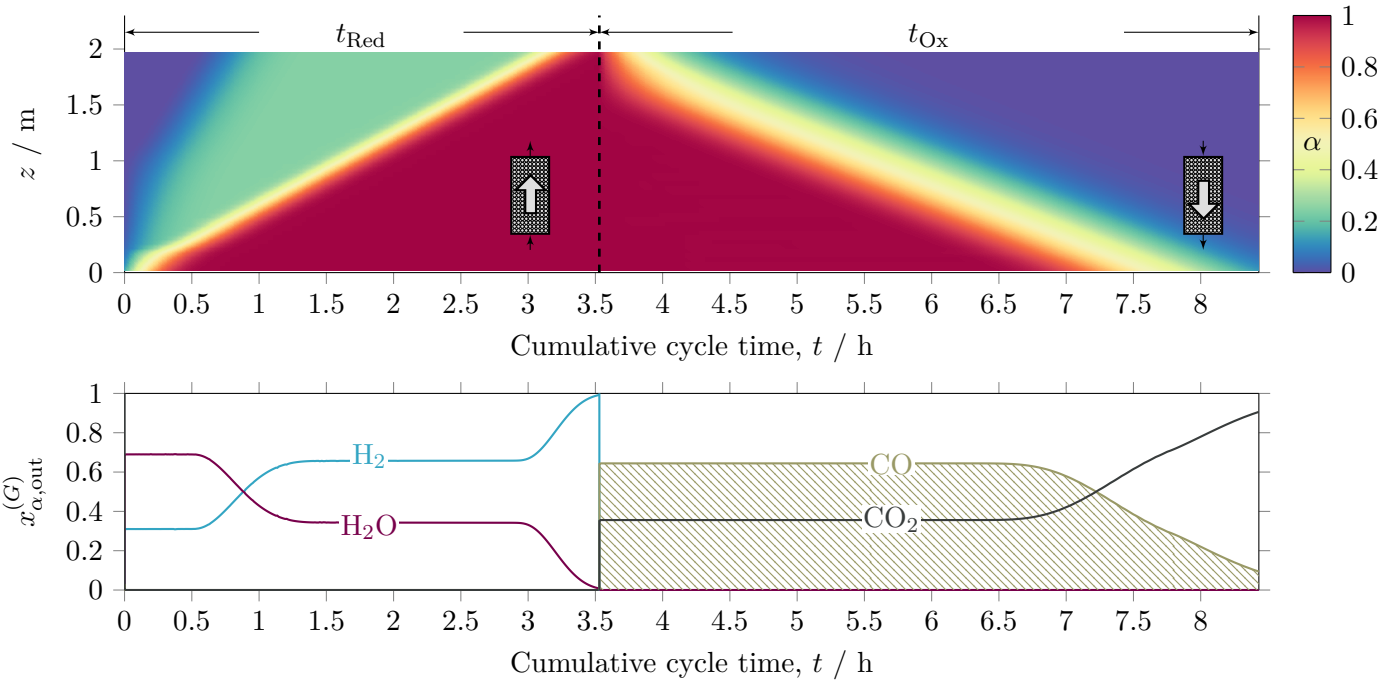

Figure 8: Reduction extent α for the fixed bed reactor design for $v^{(G)}_{\mathrm{Red}} = 2.04\,\mathrm{m/s}$, $v^{(G)}_{\mathrm{Ox}} = 1.07\,\mathrm{m/s}$, $t_{\mathrm{Red}} = 3.53\,\mathrm{h}$ and $t_{\mathrm{Ox}} = 4.90\,\mathrm{h}$ (optimization results for eq. 35) as a function of time and axial coordinate z (top) and gas outlet concentration $x^{(G)}_{\alpha,\mathrm{out}}$ as a function of time (bottom). Maximum OSM utilization is $X_{\mathrm{OSM}} = 98.6\%$ with an average CO concentration of $\bar{x}_{\mathrm{CO}} = 0.55$.

during oxidation are such that the gas composition is close to equilibrium. The optimized solution results in a maximum OSM utilization of $X_{\mathrm{OSM}} = 98.6\%$ with an average CO concentration of $\bar{x}_{\mathrm{CO}} = 0.55$. The outlet CO mole fraction stays relatively constant at $x_{\mathrm{CO,out}} = 0.64$ for the first three hours of the oxidation stage and then gradually decreases.

The maximum achievable value for $\bar{x}_{\mathrm{CO}}$ in the fixed bed case is obtained by solving equation (36). The results are shown in Figure 9. Compared to Figure 8 the reduction stage is even shorter and the gas velocity higher while the reverse is true for the oxidation stage. This leads to sharper reaction fronts during the oxidation stage, which is beneficial for obtaining high average CO concentrations. The average CO concentration under the chosen process constraints is $\bar{x}_{\mathrm{CO}} = 0.64$ since the outlet mole fraction $x_{\mathrm{CO,out}}$ is constant during oxidation. This value is limited by the equilibrium composition of the reaction from Fe to FeO (eq. (2)). However, the higher value for $\bar{x}_{\mathrm{CO}}$ is achieved at the expense of the OSM utilization, which is decreased to $X_{\mathrm{OSM}} = 83.9\%$. Even though low flow velocities during oxidation are beneficial for achieving the highest possible value for $\bar{x}_{\mathrm{CO}}$, they would result in large reactors to achieve high throughput in industrial applications.

For the fluidized bed reactor, the optimal solutions of the problems defined by equations (37) and (38)

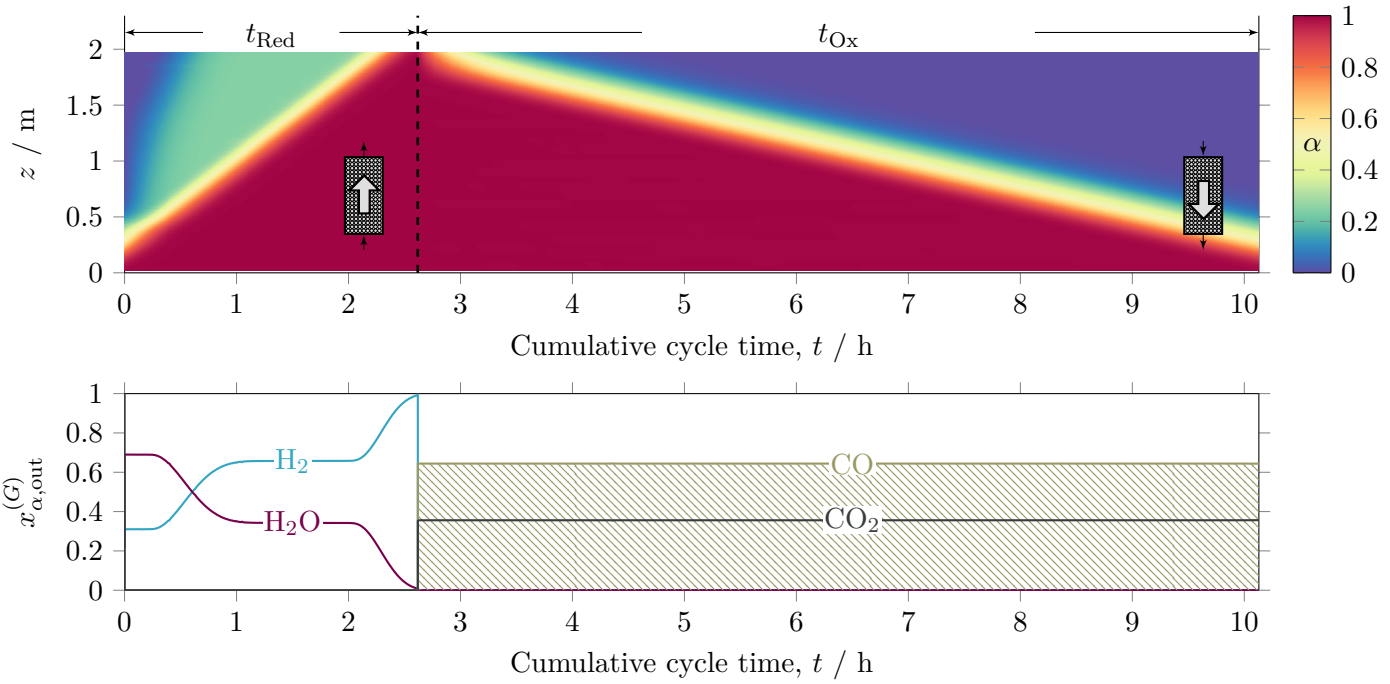

Figure 9: Reduction extent α for the fixed bed reactor design for $v^{(G)}_{\mathrm{Red}} = 2.44\,\mathrm{m/s}$, $v^{(G)}_{\mathrm{Ox}} = 0.51\,\mathrm{m/s}$, $t_{\mathrm{Red}} = 2.62\,\mathrm{h}$ and $t_{\mathrm{Ox}} = 7.51\,\mathrm{h}$ (optimization results for eq. 36) as a function of time and axial coordinate z (top) and gas outlet concentration $x^{(G)}_{\alpha,\mathrm{out}}$ as a function of time (bottom). The maximum achievable average CO concentration is $\bar{x}_{\mathrm{CO}} = 0.64$ with an OSM utilization of $X_{\mathrm{OSM}} = 83.9\%$.

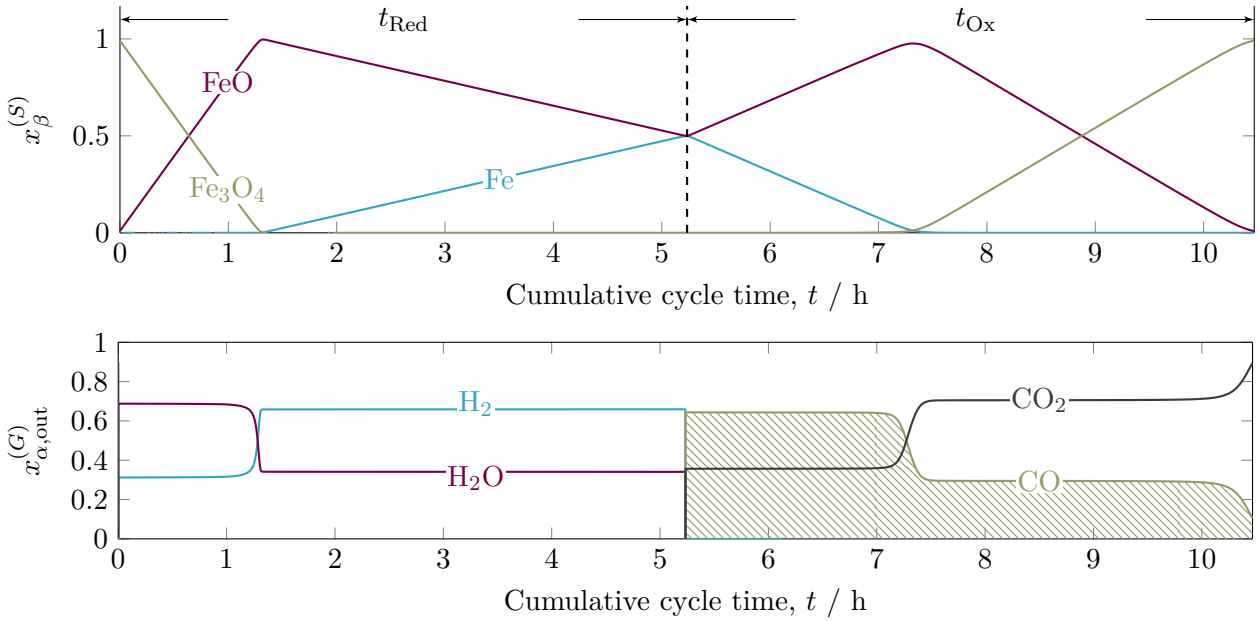

Figure 10: Solid composition $x_\beta^{(S)}$ for the fluidized bed reactor design for $v_{\mathrm{Red}}^{(G)} = v_{\mathrm{Ox}}^{(G)} = 0.6\,\mathrm{m/s}$ and $t_{\mathrm{Red}} = t_{\mathrm{Ox}} = 5.23\,\mathrm{h}$ (optimization results for eq. 37) as a function of time (top) and gas outlet concentration $x_{\alpha,\mathrm{out}}^{(G)}$ as a function of time (bottom). OSM utilization is $X_{\mathrm{OSM}} = 42.9\%$ with an average CO concentration of $\bar{x}_{\mathrm{CO}} = 0.53$.

are very similar and therefore only the solution for maximum OSM utilization is depicted in Figure 10. Maximizing the average CO concentration (equation (38)) yields slightly smaller values for t_{Red} and t_{Ox}. Thus, the final drop in the CO concentration at $t > 10\,\mathrm{h}$ seen in Figure 10 disappears. The optimum values for the two performance indicators are severely limited to $X_{\mathrm{OSM}} = 62.4\%$ and $\bar{x}_{\mathrm{CO}} = 0.429$ for the fluidized bed reactor design, respectively. This is due to two reasons: 1) the slower kinetics of reduction compared to oxidation 2) fixed gas flow velocity due to fluidization constraints limiting the degrees of freedom for process control compared to the fixed bed reactor design. Solutions where $t_{\mathrm{Red}} = t_{\mathrm{Ox}}$ are generally superior to solutions where $t_{\mathrm{Red}} < t_{\mathrm{Ox}}$, since a shorter reduction period time compared to the oxidation period time decreases the OSM utilization leading to a lower average CO concentration. Solutions with $t_{\mathrm{Red}} > t_{\mathrm{Ox}}$ would theoretically yield better results but are prohibited because in this work only two reactors are allowed. The results in Figure 10 show that during reduction, the maximum mole fraction of Fe is only $x_{\mathrm{Fe}}^{(S)} \approx 0.5$. However, during oxidation the reaction step from Fe to FeO (see eq. 2) yields the highest possible CO concentration in the gas outlet. This favorable reaction step from Fe to FeO can not be completely used under the constraints of the fluidized bed. Therefore, the average CO concentration and the OSM utilization are strongly decreased in the fluidized bed reactor case compared to the fixed bed reactor case. For higher values for $\bar{x}_{\mathrm{CO}}$ and X_{OSM}, a different OSM with more favorable kinetics or more than two reactors would be required.

Table 2: Summary of process parameters and performance criteria for the fixed and fluidized bed reactor design optimization cases defined by equations (35) to (38). In both cases, $v^{(G)}$ denotes the respective superficial gas velocity. The total amount of material in the reactor is 2059.1 kg in both cases. The conversion of H_2 during the reduction stage and of CO_2 during the oxidation stage are denoted by X_{H_2} and CO_2, respectively.

		Fixed Bed max X_{OSM}, eq. (35)	Fixed Bed max $\bar{x}_{\mathrm{CO}}$, eq. (36)	Fluidized Bed max X_{OSM}, eq. (37)	Fluidized Bed max $\bar{x}_{\mathrm{CO}}$, eq. (38)
t_{Red}	[h]	3.53	2.62	5.23	4.42
t_{Ox}	[h]	4.90	7.51	5.23	4.42
$v_{\mathrm{Red}}^{(G)}$	[m/s]	2.04	2.44	0.60	0.60
$v_{\mathrm{Ox}}^{(G)}$	[m/s]	1.07	0.51	0.60	0.60
X_{OSM}	[−]	0.986	0.839	0.624	0.531
$\bar{x}_{\mathrm{CO}}$	[−]	0.547	0.644	0.426	0.429
$X_{\mathrm{H_2}}$	[−]	0.400	0.384	0.423	0.426
$X_{\mathrm{CO_2}}$	[−]	0.547	0.644	0.423	0.426
$\dot{N}_{\mathrm{CO}}$	[kmol/h]	8.25	4.58	4.89	4.92

The results for the optimization problems (35) to (38) are summarized in Table 2. The gas conversions of H_2 during reduction (X_{H_2}) and of CO_2 during oxidation (X_{CO_2}) are given in addition to the performance criteria. Theoretically, a total amount of 25.6 kmol of CO_2 could be converted stoichiometrically with the given amount of OSM. The gas conversion of CO_2 is higher but the H_2 conversion is lower in the fixed bed reactor compared to the fluidized bed reactor. The total molar flow of CO for each case is calculated using the following equation

$$\dot{N}_{\mathrm{CO}} = \frac{4}{3}\frac{m_{\mathrm{OSM}} X_{\mathrm{OSM}}}{M^{(S)} t_{\mathrm{Ox}}}, \tag{39}$$

where m_{OSM} is the total amount of material in the reactor (2059.1 kg). It can be seen that the fixed bed reactor with maximum OSM utilization produces 8.25 $\mathrm{kmol_{CO}}$/h which is almost twice as much as the alternatives.

Figure 11 shows the Pareto plot for the fixed and fluidized bed reactor designs with regard to the two average CO concentration and the OSM utilization. The circles indicate the solution which maximizes one of the two objectives (discussed previously). As illustrated in Figure 11 the fixed bed reactor design is strictly superior to the fluidized bed reactor design with regard to both performance indicators. The maximum average CO concentration is limited by thermodynamics to 0.644 and the OSM utilization cannot be increased above 0.986 without violating the optimization constraints. The Pareto optimal front for the fluidized bed reactor design is small and nearly insensitive to changes in the OSM utilization, i.e. for all

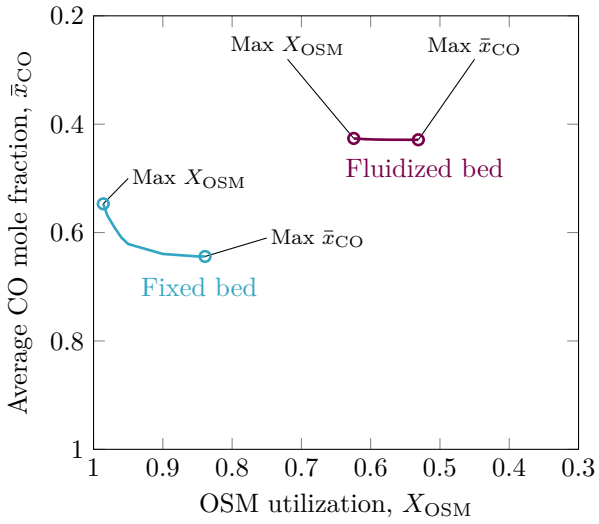

Figure 11: Pareto plot of the optimal solutions for the average CO concentration and OSM utilization for the fixed bed (blue) and fluidized bed (red) reactor designs. Circles indicate the solution, which maximizes one of the two objectives.

solutions, the average CO concentration is nearly the same. The solution of the optimization problems defined by equations (37) and (38) lie close to each other on the Pareto plot. The Pareto plot illustrates that the performance of the fluidized bed reactor design is severely limited if only two reactors are available with the investigated OSM. The fixed bed reactor allows for greater operational freedom with the control of the gas flows and therefore yields higher values for both performance indicators. However, in this study the practical challenges of operation like excessive material sintering, deactivation, elutration, attrition, etc. are not discussed.

4. Conclusions

The RWGS-CL process was mathematically described using dynamic, one dimensional models for fixed bed and fluidized bed reactor configurations assuming only two reactors each for quasi-continuous production of CO. It was shown for the fixed bed reactor that under equivalent inlet gas concentrations the reduction is slower in an equilibrium limited reaction regime and faster in a rate limited reaction regime compared to the oxidation. The equilibrium limited reaction regime is advantageous during oxidation in the fixed bed reactor case, since high CO concentrations can be reached when distinct reaction fronts are present. This result was analyzed in detail in a subsequent optimization of the process. Therefore, two performance indicators were defined, the OSM utilization and the average CO concentration. The optimization results were compared in a Pareto plot. The fixed bed reactor configuration yields better results for both performance indicators compared to the fluidized bed reactor configuration. The performance of the fluidized bed reactor design is severely limited because the gas flow velocities are fixed by the hydrodynamics and therefore the possibilities

for process are decreased. The maximum performance potential of chemical looping systems in general strongly depends on the dynamics of the system. If the regeneration stage is limiting, higher degrees of operational freedom are needed to achieve high performance. Thus, material design and selection for chemical looping processes should consider that it is important that the regeneration stage of the cycle should ideally be faster than the production stage. The insights gained from this detailed analysis are applicable to comparable chemical looping systems.

Appendix A: Fixed Bed Model Derivation

Gas Phase

Starting point for the model derivation is the local partial mass balance in one spatial dimension for the gas phase (G)

$$\frac{\partial \rho_\alpha^{(G)}}{\partial t} = -\frac{\partial}{\partial z}\left(\rho_\alpha^{(G)} v^{(G)} + j_\alpha^{(G)}\right) + \sigma_\alpha^M \qquad \forall \alpha = \{\mathrm{H_2}, \mathrm{H_2O}, \mathrm{CO}, \mathrm{CO_2}\}\,, \tag{40}$$

where $\rho_\alpha^{(G)}$ is the local mass density of component α ($\left[\rho_\alpha^{(G)}\right] = \mathrm{kg/m^3_{Reactor}}$), $v^{(G)}$ the gas phase superficial velocity, $j_\alpha^{(G)}$ the diffusive flux and σ_α^M the specific source term ($\left[\sigma_\alpha^M\right] = \mathrm{kg/m^3/s}$). Assuming that diffusion can be neglected because of high gas velocity, eq. (40) reduces to

$$\frac{\partial \rho_\alpha^{(G)}}{\partial t} = -\frac{\partial}{\partial z}\left(\rho_\alpha^{(G)} v^{(G)}\right) + \sigma_\alpha^M. \tag{41}$$

The gas phase velocity $v^{(G)}$ can be calculated starting from the local total mass balance of the gas phase

$$\frac{\partial \rho^{(G)}}{\partial t} = -\frac{\partial}{\partial z}\left(\rho^{(G)} v^{(G)}\right) \tag{42}$$

by introducing the ideal gas law and assuming isothermal and isobaric operation of the reactor. In this case, the local total mass density of the gas, $\rho^{(G)}$, is constant and eq. (42) reduces to

$$0 = \frac{\partial v^{(G)}}{\partial z}, \tag{43}$$

i.e. $v^{(G)}$ is constant throughout the reactor. The superficial gas phase velocity $v^{(G)}$ and the void fraction ε can be used to calculate the interstitial gas phase velocity $v_{\mathrm{int}}^{(G)}$ (velocity in the gas void volume) by

$$v_{\mathrm{int}}^{(G)} = \frac{v^{(G)}}{\varepsilon}. \tag{44}$$

With $\rho_\alpha^{(G)} = c_t^{(G)} M_\alpha x_\alpha^{(G)} \varepsilon$, eq. (41) can be rewritten as

$$\frac{\partial}{\partial t}\left(c_t^{(G)} M_\alpha x_\alpha^{(G)} \varepsilon\right) = -\frac{\partial}{\partial z}\left(c_t^{(G)} M_\alpha x_\alpha^{(G)} \varepsilon v_{\mathrm{int}}^{(G)}\right) + \sigma_\alpha^M = -\frac{\partial}{\partial z}\left(c_t^{(G)} M_\alpha x_\alpha^{(G)} v^{(G)}\right) + \sigma_\alpha^M, \tag{45}$$

where $c_t^{(G)}$ is the molar concentration of the gas phase, M_α the molar mass of component α, $x_\alpha^{(G)}$ the gas phase mole fraction of component α and ε the fixed bed void fraction ($[\varepsilon] = \mathrm{m}^3_{\mathrm{Gas}}/\mathrm{m}^3_{\mathrm{Reactor}}$). Here, $c_t^{(G)}$, M_α and ϵ are constant. Furthermore, the specific source term σ_α^M for the gas phase is defined as

$$\sigma_\alpha^M = M_\alpha \sum_j^{N_R} \nu_{\alpha,j} r_{j,\mathrm{eff}}. \tag{46}$$

Eq. (45) and (46) can be rearranged to yield

$$\frac{\partial x_\alpha^{(G)}}{\partial t} = -\frac{v^{(G)}}{\varepsilon}\frac{\partial x_\alpha^{(G)}}{\partial z} + \frac{1}{\varepsilon c_t^{(G)}} \sum_j^{N_R} \nu_{\alpha,j} r_{j,\mathrm{eff}}. \tag{47}$$

Here, $\nu_{\alpha,j}$ is the stoichiometric coefficient of component α in reaction j and $r_{j,\mathrm{eff}}$ is the corresponding effective reaction rate. N_R denotes the total number of reactions considered. For gas-solid reactions, the reaction rate is often expressed in terms of mol/kg/s. However, in eq. (47) the reaction rate is given as $[r_{j,\mathrm{eff}}] = \mathrm{mol/m^3/s}$. To convert between the rate expressions, the solid phase density $\rho^{(S)}$ and the fixed bed void fraction can be used according to

$$r_{j,\mathrm{eff}} = (1-\varepsilon)\rho^{(S)} r_{j,\mathrm{eff}}^M. \tag{48}$$

Here $r_{j,\mathrm{eff}}^M$ denotes the reaction rate in terms of mol/kg/s. The effective reaction rate $r_{j,\mathrm{eff}}^M$ is related to the intrinsic reaction rate r_j^M by the effectiveness factor η_{eff}:

$$r_{j,\mathrm{eff}}^M = \eta_{\mathrm{eff}} r_j^M \tag{49}$$

The effectiveness factor is introduced to account for mass transfer resistances in the pores of the oxygen storage material and the resulting decrease in reactivity. Combining equations (48) and (49) with eq. (47) yields the final balance in form of the gas mole fractions:

$$\frac{\partial x_\alpha^{(G)}}{\partial t} = -\frac{v^{(G)}}{\varepsilon}\frac{\partial x_\alpha^{(G)}}{\partial z} + \frac{(1-\varepsilon)}{\varepsilon}\frac{\rho^{(S)}}{c_t^{(G)}}\eta_{\mathrm{eff}} \sum_j^{N_R} \nu_{\alpha,j} r_j^M \qquad \forall \alpha = \{\mathrm{H_2}, \mathrm{H_2O}, \mathrm{CO}, \mathrm{CO_2}\} \tag{50}$$

Solid Phase

The derivation of the model equation for the solid phase (S) is analogous to the gas phase. The local partial mass balance in one spatial dimension for the solid phase (S) reads

$$\frac{\partial \rho_\beta^{(S)}}{\partial t} = -\frac{\partial}{\partial z}\left(\rho_\beta^{(S)} v^{(S)} + j_\beta^{(S)}\right) + \sigma_\beta^M \qquad \forall \beta = \left\{\mathrm{Fe}, \mathrm{FeO}, \mathrm{FeO_{4/3}}\right\}. \tag{51}$$

Since the solid phase is a fixed bed it follows that $v^{(S)} = 0$. Assuming that diffusion can be neglected in the solid phase, eq. (51) reduces to

$$\frac{\partial \rho_\beta^{(S)}}{\partial t} = \sigma_\beta^M. \tag{52}$$

With $\rho_\beta^{(S)} = c_t^{(S)} M_\beta x_\beta^{(S)} (1-\varepsilon)$, eq. (52) can be rewritten as

$$\frac{\partial}{\partial t}\left(c_t^{(S)} M_\beta x_\beta^{(S)} (1-\varepsilon)\right) = \sigma_\beta^M, \tag{53}$$

where $c_t^{(S)}$, M_β and ε are constant. The specific source term σ_β^M for the solid phase is defined as

$$\sigma_\beta^M = M_\beta \sum_j^{N_R} \nu_{\beta,j} r_{j,\text{eff}}. \tag{54}$$

Introducing eqs. (48) and (49) and rearranging leads to the final balance in form of the solid mole fractions:

$$\frac{\partial x_\beta^{(S)}}{\partial t} = \frac{(1-\varepsilon)\rho^{(S)}}{(1-\varepsilon)c_t^{(S)}} \eta_{\text{eff}} \sum_j^{N_R} \nu_{\beta,j} r_=^M M^{(S)} \eta_{\text{eff}} \sum_j^{N_R} \nu_{\beta,j} r_j^M \qquad \forall \beta = \left\{\text{Fe}, \text{FeO}, \text{FeO}_{4/3}\right\} \tag{55}$$

Model Discretization

The finite volume method (FVM) was used to discretize the derived model equations spatially to yield a coupled ODE system, which was solved in MATLAB (*ode15s*). Piecewise constant functions were assumed for the system variables $x_\alpha^{(G)}$ and $x_\beta^{(S)}$ and an upwind scheme was used because of the defined flow direction. The inlet condition for $x_\alpha^{(G)}$ is used as a boundary condition:

$$x_\alpha^{(G)}\Big|_{z=0} = x_{\alpha,\text{in}}^{(G)} \tag{56}$$

The discretization scheme with equidistant spacing of the finite volumes is illustrated in Figure 12. The following ODE system is derived:

$$\frac{\mathrm{d}x_{\alpha,1}^{(G)}}{\mathrm{d}t} = -\frac{v^{(G)}}{\varepsilon \Delta z}\left(x_{\alpha,1}^{(G)} - x_{\alpha,\text{in}}^{(G)}\right) + \frac{(1-\varepsilon)}{\varepsilon}\frac{\rho^{(S)}}{c_t^{(G)}} \eta_{\text{eff}} \sum_j^{N_R} \nu_{\alpha,j} r_j^M (x_{\alpha,1}^{(G)}, x_{\beta,1}^{(S)}) \tag{57}$$

$$\frac{\mathrm{d}x_{\alpha,i}^{(G)}}{\mathrm{d}t} = -\frac{v^{(G)}}{\varepsilon \Delta z}\left(x_{\alpha,i}^{(G)} - x_{\alpha,i-1}^{(G)}\right) + \frac{(1-\varepsilon)}{\varepsilon}\frac{\rho^{(S)}}{c_t^{(G)}} \eta_{\text{eff}} \sum_j^{N_R} \nu_{\alpha,j} r_j^M (x_{\alpha,i}^{(G)}, x_{\beta,i}^{(S)}) \qquad \forall i = 2 \ldots N_{FV} \tag{58}$$

$$\frac{\mathrm{d}x_{\beta,i}^{(S)}}{\mathrm{d}t} = M^{(S)} \eta_{\text{eff}} \sum_j^{N_R} \nu_{\beta,j} r_j^M (x_{\alpha,i}^{(G)}, x_{\beta,i}^{(S)}) \qquad \forall i = 1 \ldots N_{FV} \tag{59}$$

Here, i indicates the number of finite volumes ranging from 1 to N_{FV}. In this study, 50 finite elements were used for simulation and optimization. This number was found to be most efficient while granting accurate results.

Appendix B: Two-Region Fluidized Bed Model Derivation

Bubble Region

The local partial mass balance in one spatial dimension for the gas phase in the bubble region (b) can be stated as follows:

$$\frac{\partial \rho_\alpha^{(b)}}{\partial t} = -\frac{\partial}{\partial z}\left(\rho_\alpha^{(b)} v^{(b)} + j_\alpha^{(b)}\right) + \sigma_\alpha^M \qquad \forall \alpha = \left\{\text{H}_2, \text{H}_2\text{O}, \text{CO}, \text{CO}_2\right\}, \tag{60}$$

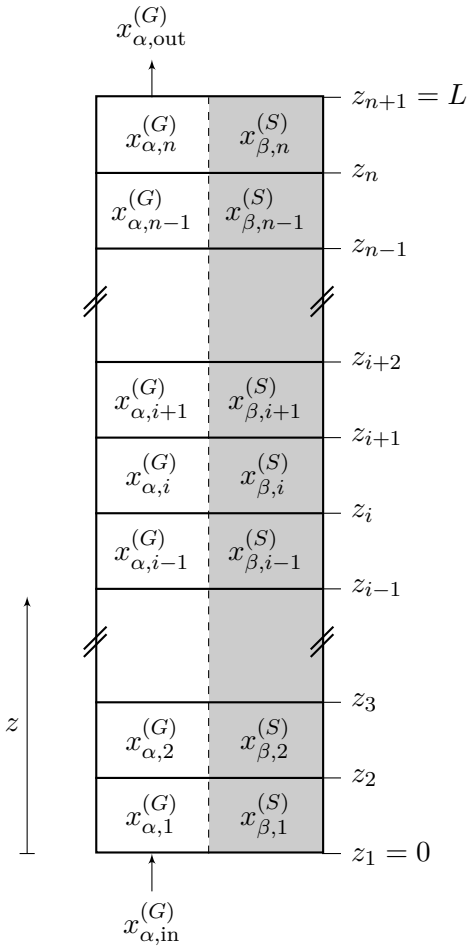

Figure 12: Discretization scheme for the fixed bed reactor model.

where $\rho_\alpha^{(b)}$ is the local mass density of component α ($\left[\rho_\alpha^{(b)}\right] = \mathrm{kg/m^3_{Reactor}}$), $v^{(b)}$ the rise velocity of bubble gas, $j_\alpha^{(b)}$ the diffusive flux and σ_α^M the specific source term ($\left[\sigma_\alpha^M\right] = \mathrm{kg/m^3/s}$). Assuming that diffusion can be neglected because of high gas velocity and that no reaction occurs in the bubble region, eq. (60) reduces to

$$\frac{\partial \rho_\alpha^{(b)}}{\partial t} = -\frac{\partial}{\partial z}\left(\rho_\alpha^{(b)} v^{(b)}\right). \tag{61}$$

With $\rho_\alpha^{(b)} = c_\alpha^{(b)} M_\alpha \delta$, eq. (61) can be rewritten as

$$\frac{\partial}{\partial t}\left(c_\alpha^{(b)} M_\alpha \delta\right) = -\frac{\partial}{\partial z}\left(c_\alpha^{(b)} M_\alpha \delta v^{(b)}\right), \tag{62}$$

where $c_t^{(b)}$ is the molar concentration of component α in the gas of the bubble region, M_α the molar mass of component α and δ the bubble fraction ($[\delta] = \mathrm{m^3_{Bubble}/m^3_{Reactor}}$). Here, M_α, δ and $v^{(b)}$ are assumed to be constant. Furthermore, a bubble-emulsion mass interchange term is inserted to describe the mass flow between the two regions:

$$\delta \frac{\partial c_\alpha^{(b)}}{\partial t} = -\delta v^{(b)} \frac{\partial c_\alpha^{(b)}}{\partial z} - \delta K^{(be)}\left(c_\alpha^{(b)} - c_\alpha^{(e)}\right) \tag{63}$$

Here, $K^{(be)}$ denotes the bubble-emulsion gas interchange coefficient ($\left[K^{(be)}\right] = 1/\mathrm{s}$) and $c_\alpha^{(e)}$ the molar gas concentration in the emulsion region. It is assumed that the ideal gas law holds, such that the total gas concentration in both regions is equal:

$$c_t^{(b)} = c_t^{(e)} = c_t^{(G)} \tag{64}$$

Rearranging yields the final equation in form of the gas phase mole fractions in the bubble region:

$$\frac{\partial x_\alpha^{(b)}}{\partial t} = -v^{(b)} \frac{\partial x_\alpha^{(b)}}{\partial z} - K^{(be)}\left(x_\alpha^{(b)} - x_\alpha^{(e)}\right) \tag{65}$$

Emulsion Region

Gas Phase

For the gas phase in the emulsion region (e), a similar derivation is used starting from the local partial mass balance in one spatial dimension:

$$\frac{\partial \rho_\alpha^{(e)}}{\partial t} = -\frac{\partial}{\partial z}\left(\rho_\alpha^{(e)} v^{(e)} + j_\alpha^{(e)}\right) + \sigma_\alpha^M \qquad \forall \alpha = \{\mathrm{H_2}, \mathrm{H_2O}, \mathrm{CO}, \mathrm{CO_2}\}, \tag{66}$$

where $\rho_\alpha^{(e)}$ is the local mass density of component α ($\left[\rho_\alpha^{(e)}\right] = \mathrm{kg/m^3_{Reactor}}$), $v^{(e)}$ the emulsion region gas velocity, $j_\alpha^{(e)}$ the diffusive flux and σ_α^M the specific source term ($\left[\sigma_\alpha^M\right] = \mathrm{kg/m^3/s}$). Assuming that diffusion can be neglected because of high gas velocity, eq. (66) reduces to

$$\frac{\partial \rho_\alpha^{(e)}}{\partial t} = -\frac{\partial}{\partial z}\left(\rho_\alpha^{(e)} v^{(e)}\right) + \sigma_\alpha^M. \tag{67}$$

With $\rho_\alpha^{(e)} = c_\alpha^{(e)} M_\alpha (1-\delta)\varepsilon_{\mathrm{mf}}$ and eq. (46), eq. (67) can be rewritten as

$$\frac{\partial}{\partial t}\left(c_\alpha^{(e)} M_\alpha (1-\delta)\varepsilon_{\mathrm{mf}}\right) = -\frac{\partial}{\partial z}\left(c_\alpha^{(e)} M_\alpha (1-\delta)\varepsilon_{\mathrm{mf}} v^{(e)}\right) + M_\alpha \sum_j^{N_R} \nu_{\alpha,j} r_j. \tag{68}$$

Here, $\varepsilon_{\mathrm{mf}}$ denotes the minimum fluidization void fraction ($[\varepsilon_{\mathrm{mf}}] = \mathrm{m}^3_{\mathrm{Gas}}/\mathrm{m}^3_{\mathrm{Emulsion}}$). In fluidized bed operation, the effectiveness factor η_{eff} is assumed to be unity, such that $r_{j,\mathrm{eff}}^M = r_j^M$. This assumption is realistic because in fluidized bed reactors the mass and heat transfer resistance is minimized by vigorous mixing and a small particle size [36]. To convert from $[r_j] = \mathrm{mol/m^3/s}$ to $\left[r_j^M\right] = \mathrm{mol/kg/s}$, the following equation is used:

$$r_j = (1-\delta)(1-\varepsilon_{\mathrm{mf}})\rho^{(S)} r_j^M \tag{69}$$

Rearranging eq. (68) yields:

$$(1-\delta)\varepsilon_{\mathrm{mf}}\frac{\partial c_\alpha^{(e)}}{\partial t} = -(1-\delta)\varepsilon_{\mathrm{mf}} v^{(e)}\frac{\partial c_\alpha^{(e)}}{\partial z} + (1-\delta)(1-\varepsilon_{\mathrm{mf}})\rho^{(S)}\sum_j^{N_R}\nu_{\alpha,j} r_j^M. \tag{70}$$

Again, a bubble-emulsion mass interchange term is inserted to describe the mass flow between the two regions:

$$(1-\delta)\varepsilon_{\mathrm{mf}}\frac{\partial c_\alpha^{(e)}}{\partial t} = -(1-\delta)\varepsilon_{\mathrm{mf}} v^{(e)}\frac{\partial c_\alpha^{(e)}}{\partial z} + \delta K^{(be)}\left(c_\alpha^{(b)} - c_\alpha^{(e)}\right) + (1-\delta)(1-\varepsilon_{\mathrm{mf}})\rho^{(S)}\sum_j^{N_R}\nu_{\alpha,j} r_j^M \tag{71}$$

Using eq. (64) and rearranging, the final equation in form of the gas phase mole fractions in the emulsion region:

$$\frac{\partial x_\alpha^{(e)}}{\partial t} = -v^{(e)}\frac{\partial x_\alpha^{(e)}}{\partial z} + \frac{\delta}{(1-\delta)\varepsilon_{\mathrm{mf}}} K^{(be)}\left(x_\alpha^{(b)} - x_\alpha^{(e)}\right) + \frac{1-\varepsilon_{\mathrm{mf}}}{\varepsilon_{\mathrm{mf}}}\frac{\rho^{(S)}}{c_t^{(G)}}\sum_j^{N_R}\nu_{\alpha,j} r_j^M \tag{72}$$

Solid Phase

For the solid phase in the emulsion region (S), the dispersion model is used according to Kunii and Levenspiel [31] with an additional reaction term:

$$\frac{\partial \rho_\beta^{(S)}}{\partial t} = D_v^{(S)}\frac{\partial^2 \rho_\beta^{(S)}}{\partial z^2} + \sigma_\beta^M \qquad \forall \beta = \left\{\mathrm{Fe}, \mathrm{FeO}, \mathrm{FeO_{4/3}}\right\}, \tag{73}$$

where $\rho_\beta^{(S)}$ is the local mass density of component β ($\left[\rho_\beta^{(S)}\right] = \mathrm{kg/m^3_{Reactor}}$), $D_v^{(S)}$ the average vertical dispersion coefficient for the solid and σ_β^M the specific source term ($\left[\sigma_\beta^M\right] = \mathrm{kg/m^3/s}$).With $\rho_\beta^{(S)} = c_t^{(S)} x_\beta^{(S)} M_\beta (1-\varepsilon_{\mathrm{mf}})(1-\delta)$, eq. (73) can be rearranged to

$$\frac{\partial}{\partial t}\left(c_t^{(S)} x_\beta^{(S)} M_\beta (1-\varepsilon_{\mathrm{mf}})(1-\delta)\right) = D_v^{(S)}\frac{\partial^2}{\partial z^2}\left(c_t^{(S)} x_\beta^{(S)} M_\beta (1-\varepsilon_{\mathrm{mf}})(1-\delta)\right) + \sigma_\beta^M, \tag{74}$$

where $c_t^{(S)}$ is the total concentration of the solid. Eq. (54) is introduced to describe the reaction term:

$$\frac{\partial}{\partial t}\left(c_t^{(S)} x_\beta^{(S)} M_\beta (1-\varepsilon_{\mathrm{mf}})(1-\delta)\right) = D_v^{(S)} \frac{\partial^2}{\partial z^2}\left(c_t^{(S)} x_\beta^{(S)} M_\beta (1-\varepsilon_{\mathrm{mf}})(1-\delta)\right) + M_\beta \sum_j^{N_R} \nu_{\beta,j} r_j. \tag{75}$$

To convert from $[r_j] = \mathrm{mol/m^3/s}$ to $\left[r_j^M\right] = \mathrm{mol/kg/s}$, eq. (69) is used. Rearranging yields:

$$\frac{\partial x_\beta^{(S)}}{\partial t} = D_v^{(S)} \frac{\partial^2 x_\beta^{(S)}}{\partial z^2} + \frac{\rho^{(S)}}{c_t^{(S)}} \sum_j^{N_R} \nu_{\beta,j} r_j^M. \tag{76}$$

Noting that $\rho^{(S)}/c_t^{(S)} = M^{(S)}$ yields the final equation in form of the solid phase mole fractions in the emulsion region:

$$\frac{\partial x_\beta^{(S)}}{\partial t} = D_v^{(S)} \frac{\partial^2 x_\beta^{(S)}}{\partial z^2} + M^{(S)} \sum_j^{N_R} \nu_{\beta,j} r_j^M \tag{77}$$

Model Discretization

The finite volume method (FVM) was used to discretize the derived model equations spatially to yield a coupled ODE system, which was solved in MATLAB (*ode15s*). Piecewise constant functions were assumed for the system variables $x_\alpha^{(b)}$, $x_\alpha^{(e)}$ and $x_\beta^{(S)}$ and an upwind scheme was used because of the defined flow direction. Dispersion was assumed to be limited inside the reactor, such that the following boundary conditions for $x_\beta^{(S)}$ (no axial dispersion at the reactor inlet and outlet) can be formulated:

$$\left.\frac{\partial x_\beta^{(S)}}{\partial z}\right|_{z=0} = 0 \tag{78}$$

$$\left.\frac{\partial x_\beta^{(S)}}{\partial z}\right|_{z=L} = 0 \tag{79}$$

For $x_\alpha^{(b)}$ and $x_\alpha^{(e)}$ the inlet conditions are used as boundary conditions. The discretization scheme with equidistant spacing of the finite volumes is illustrated in Figure 13.

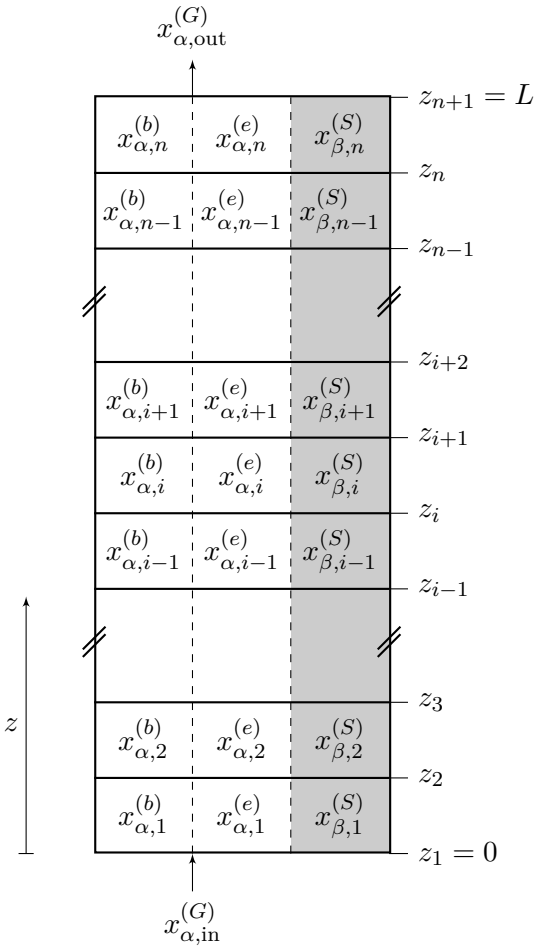

Figure 13: Discretization scheme for the two-region fluidized bed reactor model.

The following ODE system is derived:

$$\frac{\partial x_{\alpha,1}^{(b)}}{\partial t} = -\frac{v^{(b)}}{\Delta z}\left(x_{\alpha,1}^{(b)} - x_{\alpha,\text{in}}^{(G)}\right) - K^{(be)}(x_{\alpha,1}^{(b)} - x_{\alpha,1}^{(e)}) \tag{80}$$

$$\frac{\partial x_{\alpha,i}^{(b)}}{\partial t} = -\frac{v^{(b)}}{\Delta z}\left(x_{\alpha,i}^{(b)} - x_{\alpha,i-1}^{(b)}\right) - K^{(be)}(x_{\alpha,i}^{(b)} - x_{\alpha,i}^{(e)}) \qquad \forall i = 2 \dots N_{FV} \tag{81}$$

$$\begin{aligned}\frac{\partial x_{\alpha,1}^{(e)}}{\partial t} = &-\frac{v^{(e)}}{\Delta z}\left(x_{\alpha,1}^{(e)} - x_{\alpha,\text{in}}^{(G)}\right) + \frac{\delta}{(1-\delta)\varepsilon_{\text{mf}}}K^{(be)}(x_{\alpha,1}^{(b)} - x_{\alpha,1}^{(e)}) \dots \\ &+ \frac{1-\varepsilon_{\text{mf}}}{\varepsilon_{\text{mf}}}\frac{\rho^{(S)}}{c_t^{(G)}}\sum_j^{N_R}\nu_{\alpha,j}r_j^M(x_{\alpha,1}^{(e)}, x_{\beta,1}^{(S)})\end{aligned} \tag{82}$$

$$\begin{aligned}\frac{\partial x_{\alpha,i}^{(e)}}{\partial t} = &-\frac{v^{(e)}}{\Delta z}\left(x_{\alpha,i}^{(e)} - x_{\alpha,i-1}^{(e)}\right) + \frac{\delta}{(1-\delta)\varepsilon_{\text{mf}}}K^{(be)}(x_{\alpha,i}^{(b)} - x_{\alpha,i}^{(e)}) \dots \\ &+ \frac{1-\varepsilon_{\text{mf}}}{\varepsilon_{\text{mf}}}\frac{\rho^{(S)}}{c_t^{(G)}}\sum_j^{N_R}\nu_{\alpha,j}r_j^M(x_{\alpha,i}^{(e)}, x_{\beta,i}^{(S)}) \qquad \forall i = 2 \dots N_{FV}\end{aligned} \tag{83}$$

$$\frac{\partial x_{\beta,1}^{(S)}}{\partial t} = \frac{D_v^{(S)}}{\Delta z^2}\left(x_{\beta,2}^{(S)} - x_{\beta,1}^{(S)}\right) + M^{(S)}\sum_j^{N_R}\nu_{\beta,j}r_j^M(x_{\alpha,1}^{(e)}, x_{\beta,1}^{(S)}) \tag{84}$$

$$\frac{\partial x_{\beta,i}^{(S)}}{\partial t} = \frac{D_v^{(S)}}{\Delta z^2}\left(x_{\beta,i+1}^{(S)} - 2x_{\beta,i}^{(S)} + x_{\beta,i-1}^{(S)}\right) + M^{(S)}\sum_j^{N_R}\nu_{\beta,j}r_j^M(x_{\alpha,i}^{(e)}, x_{\beta,i}^{(S)}) \qquad \forall i = 2 \dots N_{FV} - 1 \tag{85}$$

$$\frac{\partial x_{\beta,n}^{(S)}}{\partial t} = -\frac{D_v^{(S)}}{\Delta z^2}\left(x_{\beta,n}^{(S)} - x_{\beta,n-1}^{(S)}\right) + M^{(S)}\sum_j^{N_R}\nu_{\beta,j}r_j^M(x_{\alpha,n}^{(e)}, x_{\beta,n}^{(S)}) \tag{86}$$

Here, i indicates the number of finite volumes ranging from 1 to N_{FV}. In this study, 50 finite elements were used for simulation and optimization. This number was found to be most efficient while granting accurate results.

Appendix C: Reaction Kinetics

The oxidation and reduction stage each proceed in two consecutive reaction steps through the intermediate product FeO according to the following reaction equations:

$$\text{Oxidation step 1:} \quad \text{Fe} + \text{CO}_2 \rightleftharpoons \text{FeO} + \text{CO} \qquad \Delta H_R(1073K) = 15.12\,\text{kJ/mol} \tag{87}$$

$$\text{Oxidation step 2:} \quad \text{FeO} + 1/3\,\text{CO}_2 \rightleftharpoons \text{FeO}_{4/3} + 1/3\,\text{CO} \qquad \Delta H_R(1073K) = -3.15\,\text{kJ/mol} \tag{88}$$

$$\text{Reduction step 1:} \quad \text{FeO}_{4/3} + 1/3\,\text{H}_2 \rightleftharpoons \text{FeO} + 1/3\,\text{H}_2\text{O} \qquad \Delta H_R(1073K) = 15.43\,\text{kJ/mol} \tag{89}$$

$$\text{Reduction step 2:} \quad \text{FeO} + \text{H}_2 \rightleftharpoons \text{Fe} + \text{H}_2\text{O} \qquad \Delta H_R(1073K) = 21.72\,\text{kJ/mol} \tag{90}$$

The reaction rate expressions are formulated to account for the equilibrium limitations of this system. Unlike conventional equilibrium reaction rate expressions for equilibrium limited gas phase reactions, the rates are pieceswise defined because the forward and backward rates depend not only on the gas composition but also

on the solid oxidation state.

$$r_1^M = \begin{cases} k_{1+}^0 \cdot \exp\left(\frac{-E_{A,1+}}{RT}\right) \cdot \left(x_{\mathrm{Fe}}^{(S)}\right)^{n_{1+}} \cdot Y_{\mathrm{C}} \left(y_{\mathrm{CO_2}}^{(G)} - \frac{y_{\mathrm{CO}}^{(G)}}{K_{\mathrm{eq},1}}\right)^{m_{1+}}, & \text{if } \frac{y_{\mathrm{CO}}^{(G)}}{y_{\mathrm{CO_2}}^{(G)}} < K_{\mathrm{eq},1} \\ -k_{1-}^0 \cdot \exp\left(\frac{-E_{A,1-}}{RT}\right) \cdot \left(x_{\mathrm{FeO}}^{(S)}\right)^{n_{1-}} \cdot Y_{\mathrm{C}} \left(\frac{y_{\mathrm{CO}}^{(G)}}{K_{\mathrm{eq},1}} - y_{\mathrm{CO_2}}^{(G)}\right)^{m_{1-}}, & \text{if } \frac{y_{\mathrm{CO}}^{(G)}}{y_{\mathrm{CO_2}}^{(G)}} > K_{\mathrm{eq},1} \end{cases} \tag{91}$$

$$r_2^M = \begin{cases} k_{2+}^0 \cdot \exp\left(\frac{-E_{A,2+}}{RT}\right) \cdot \left(x_{\mathrm{FeO}}^{(S)}\right)^{n_{2+}} \cdot Y_{\mathrm{C}} \left(y_{\mathrm{CO_2}}^{(G)} - \frac{y_{\mathrm{CO}}^{(G)}}{K_{\mathrm{eq},2}}\right)^{m_{2+}}, & \text{if } \frac{y_{\mathrm{CO}}^{(G)}}{y_{\mathrm{CO_2}}^{(G)}} < K_{\mathrm{eq},2} \\ -k_{2-}^0 \cdot \exp\left(\frac{-E_{A,2-}}{RT}\right) \cdot \left(x_{\mathrm{FeO_{4/3}}}^{(S)}\right)^{n_{2-}} \cdot Y_{\mathrm{C}} \left(\frac{y_{\mathrm{CO}}^{(G)}}{K_{\mathrm{eq},2}} - y_{\mathrm{CO_2}}^{(G)}\right)^{m_{2-}}, & \text{if } \frac{y_{\mathrm{CO}}^{(G)}}{y_{\mathrm{CO_2}}^{(G)}} > K_{\mathrm{eq},2} \end{cases} \tag{92}$$

$$r_3^M = \begin{cases} k_{3+}^0 \cdot \exp\left(\frac{-E_{A,3+}}{RT}\right) \cdot \left(x_{\mathrm{FeO_{4/3}}}^{(S)}\right)^{n_{3+}} \cdot Y_{\mathrm{H}} \left(y_{\mathrm{H_2}}^{(G)} - \frac{y_{\mathrm{H_2O}}^{(G)}}{K_{\mathrm{eq},3}}\right)^{m_{3+}}, & \text{if } \frac{y_{\mathrm{H_2O}}^{(G)}}{y_{\mathrm{H_2}}^{(G)}} < K_{\mathrm{eq},3} \\ -k_{3-}^0 \cdot \exp\left(\frac{-E_{A,3-}}{RT}\right) \cdot \left(x_{\mathrm{FeO}}^{(S)}\right)^{n_{3-}} \cdot Y_{\mathrm{H}} \left(\frac{y_{\mathrm{H_2O}}^{(G)}}{K_{\mathrm{eq},3}} - y_{\mathrm{H_2}}^{(G)}\right)^{m_{3-}}, & \text{if } \frac{y_{\mathrm{H_2O}}^{(G)}}{y_{\mathrm{H_2}}^{(G)}} > K_{\mathrm{eq},3} \end{cases} \tag{93}$$

$$r_4^M = \begin{cases} k_{4+}^0 \cdot \exp\left(\frac{-E_{A,4+}}{RT}\right) \cdot \left(x_{\mathrm{FeO}}^{(S)}\right)^{n_{4+}} \cdot Y_{\mathrm{H}} \left(y_{\mathrm{H_2}}^{(G)} - \frac{y_{\mathrm{H_2O}}^{(G)}}{K_{\mathrm{eq},4}}\right)^{m_{4+}}, & \text{if } \frac{y_{\mathrm{H_2O}}^{(G)}}{y_{\mathrm{H_2}}^{(G)}} < K_{\mathrm{eq},4} \\ -k_{4-}^0 \cdot \exp\left(\frac{-E_{A,4-}}{RT}\right) \cdot \left(x_{\mathrm{Fe}}^{(S)}\right)^{n_{4-}} \cdot Y_{\mathrm{H}} \left(\frac{y_{\mathrm{H_2O}}^{(G)}}{K_{\mathrm{eq},4}} - y_{\mathrm{H_2}}^{(G)}\right)^{m_{4-}}, & \text{if } \frac{y_{\mathrm{H_2O}}^{(G)}}{y_{\mathrm{H_2}}^{(G)}} > K_{\mathrm{eq},4} \end{cases} \tag{94}$$

Here, ratios of the mole fractions of CO/CO_2 and H_2/H_2O denoted by y_i are introduced, which are defined as follows:

$$y_{\mathrm{CO}}^{(G)} = \frac{x_{\mathrm{CO}}^{(G)}}{x_{\mathrm{CO}}^{(G)} + x_{\mathrm{CO_2}}^{(G)}} \tag{95}$$

$$y_{\mathrm{CO_2}}^{(G)} = \frac{x_{\mathrm{CO_2}}^{(G)}}{x_{\mathrm{CO}}^{(G)} + x_{\mathrm{CO_2}}^{(G)}} \tag{96}$$

$$y_{\mathrm{H_2}}^{(G)} = \frac{x_{\mathrm{H_2}}^{(G)}}{x_{\mathrm{H_2}}^{(G)} + x_{\mathrm{H_2O}}^{(G)}} \tag{97}$$

$$y_{\mathrm{H_2O}}^{(G)} = \frac{x_{\mathrm{H_2O}}^{(G)}}{x_{\mathrm{H_2}}^{(G)} + x_{\mathrm{H_2O}}^{(G)}} \tag{98}$$

Furthermore, the carbon and hydrogen content is defined by Y_C and Y_H, respectively:

$$Y_C = x_{\mathrm{CO}}^{(G)} + x_{\mathrm{CO_2}}^{(G)} \tag{99}$$

$$Y_H = x_{\mathrm{H_2}}^{(G)} + x_{\mathrm{H_2O}}^{(G)} \tag{100}$$

The necessary parameters for the kinetics are taken from Wenzel *et al.* [3]. It is assumed that the two reaction steps for the oxidation (equations (91) and (92)) and reduction (equations (93) and (94)) can be described by the same reaction mechanism and therefore the same reaction parameters can be used. Furthermore, the same reaction parameters are used for the forward and backward reaction rate for each reaction. This is an approximation which is used due to the lack of more detailed information about the

reaction mechanism of each reaction step. Thus, the reaction rate equations can be simplified to

$$r_1^M = \begin{cases} k_O^0 \cdot \exp\left(\frac{-E_{A,O}}{RT}\right) \cdot \left(x_{\mathrm{Fe}}^{(S)}\right)^{n_O} \cdot Y_{\mathrm{C}} \left(y_{\mathrm{CO_2}}^{(G)} - \frac{y_{\mathrm{CO}}^{(G)}}{K_{\mathrm{eq},1}}\right)^{m_O}, & \text{if } \frac{y_{\mathrm{CO}}^{(G)}}{y_{\mathrm{CO_2}}^{(G)}} < K_{\mathrm{eq},1} \\ -k_O^0 \cdot \exp\left(\frac{-E_{A,O}}{RT}\right) \cdot \left(x_{\mathrm{FeO}}^{(S)}\right)^{n_O} \cdot Y_{\mathrm{C}} \left(\frac{y_{\mathrm{CO}}^{(G)}}{K_{\mathrm{eq},1}} - y_{\mathrm{CO_2}}^{(G)}\right)^{m_O}, & \text{if } \frac{y_{\mathrm{CO}}^{(G)}}{y_{\mathrm{CO_2}}^{(G)}} > K_{\mathrm{eq},1} \end{cases} \tag{101}$$

$$r_2^M = \begin{cases} k_O^0 \cdot \exp\left(\frac{-E_{A,O}}{RT}\right) \cdot \left(x_{\mathrm{FeO}}^{(S)}\right)^{n_O} \cdot Y_{\mathrm{C}} \left(y_{\mathrm{CO_2}}^{(G)} - \frac{y_{\mathrm{CO}}^{(G)}}{K_{\mathrm{eq},2}}\right)^{m_O}, & \text{if } \frac{y_{\mathrm{CO}}^{(G)}}{y_{\mathrm{CO_2}}^{(G)}} < K_{\mathrm{eq},2} \\ -k_O^0 \cdot \exp\left(\frac{-E_{A,O}}{RT}\right) \cdot \left(x_{\mathrm{FeO_{4/3}}}^{(S)}\right)^{n_O} \cdot Y_{\mathrm{C}} \left(\frac{y_{\mathrm{CO}}^{(G)}}{K_{\mathrm{eq},2}} - y_{\mathrm{CO_2}}^{(G)}\right)^{m_O}, & \text{if } \frac{y_{\mathrm{CO}}^{(G)}}{y_{\mathrm{CO_2}}^{(G)}} > K_{\mathrm{eq},2} \end{cases} \tag{102}$$

$$r_3^M = \begin{cases} k_R^0 \cdot \exp\left(\frac{-E_{A,R}}{RT}\right) \cdot \left(x_{\mathrm{FeO_{4/3}}}^{(S)}\right)^{n_R} \cdot Y_{\mathrm{H}} \left(y_{\mathrm{H_2}}^{(G)} - \frac{y_{\mathrm{H_2O}}^{(G)}}{K_{\mathrm{eq},3}}\right)^{m_R}, & \text{if } \frac{y_{\mathrm{H_2O}}^{(G)}}{y_{\mathrm{H_2}}^{(G)}} < K_{\mathrm{eq},3} \\ -k_R^0 \cdot \exp\left(\frac{-E_{A,R}}{RT}\right) \cdot \left(x_{\mathrm{FeO}}^{(S)}\right)^{n_R} \cdot Y_{\mathrm{H}} \left(\frac{y_{\mathrm{H_2O}}^{(G)}}{K_{\mathrm{eq},3}} - y_{\mathrm{H_2}}^{(G)}\right)^{m_R}, & \text{if } \frac{y_{\mathrm{H_2O}}^{(G)}}{y_{\mathrm{H_2}}^{(G)}} > K_{\mathrm{eq},3} \end{cases} \tag{103}$$

$$r_4^M = \begin{cases} k_R^0 \cdot \exp\left(\frac{-E_{A,R}}{RT}\right) \cdot \left(x_{\mathrm{FeO}}^{(S)}\right)^{n_R} \cdot Y_{\mathrm{H}} \left(y_{\mathrm{H_2}}^{(G)} - \frac{y_{\mathrm{H_2O}}^{(G)}}{K_{\mathrm{eq},4}}\right)^{m_R}, & \text{if } \frac{y_{\mathrm{H_2O}}^{(G)}}{y_{\mathrm{H_2}}^{(G)}} < K_{\mathrm{eq},4} \\ -k_R^0 \cdot \exp\left(\frac{-E_{A,R}}{RT}\right) \cdot \left(x_{\mathrm{Fe}}^{(S)}\right)^{n_R} \cdot Y_{\mathrm{H}} \left(\frac{y_{\mathrm{H_2O}}^{(G)}}{K_{\mathrm{eq},4}} - y_{\mathrm{H_2}}^{(G)}\right)^{m_R}, & \text{if } \frac{y_{\mathrm{H_2O}}^{(G)}}{y_{\mathrm{H_2}}^{(G)}} > K_{\mathrm{eq},4} \end{cases} \tag{104}$$

where k^0, E_A, n and m are kinetic constants for the oxidation (index O) and reduction (index R) reactions. The parameter values are given in Table 1. The piecewise definition of the rate expressions can lead to excessively long computation times or convergence problems for implicit ODE solvers because the function is not differentiable (even though it is continuous) at chemical equilibrium. Therefore, the piecewise definition of equations (101)-(104) is substituted by a differentiable function, that approximates the original equations. A sigmoid function is introduced as follows:

$$r_1^M = r_{1+}^M \cdot \left(0.5 + 0.5 \frac{y_{\mathrm{CO}} - \frac{1}{1+K_{\mathrm{eq},1}}}{\sqrt{\left(y_{\mathrm{CO}} - \frac{1}{1+K_{\mathrm{eq},1}}\right)^2 + \eta}}\right) + r_{1-}^M \cdot \left(0.5 - 0.5 \frac{y_{\mathrm{CO}} - \frac{1}{1+K_{\mathrm{eq},1}}}{\sqrt{\left(y_{\mathrm{CO}} - \frac{1}{1+K_{\mathrm{eq},1}}\right)^2 + \eta}}\right) \tag{105}$$

$$r_2^M = r_{2+}^M \cdot \left(0.5 + 0.5 \frac{y_{\mathrm{CO}} - \frac{1}{1+K_{\mathrm{eq},2}}}{\sqrt{\left(y_{\mathrm{CO}} - \frac{1}{1+K_{\mathrm{eq},2}}\right)^2 + \eta}}\right) + r_{2-}^M \cdot \left(0.5 - 0.5 \frac{y_{\mathrm{CO}} - \frac{1}{1+K_{\mathrm{eq},2}}}{\sqrt{\left(y_{\mathrm{CO}} - \frac{1}{1+K_{\mathrm{eq},2}}\right)^2 + \eta}}\right) \tag{106}$$

$$r_3^M = r_{3+}^M \cdot \left(0.5 + 0.5 \frac{y_{\mathrm{H_2O}} - \frac{1}{1+K_{\mathrm{eq},3}}}{\sqrt{\left(y_{\mathrm{H_2O}} - \frac{1}{1+K_{\mathrm{eq},3}}\right)^2 + \eta}}\right) + r_{3-}^M \cdot \left(0.5 - 0.5 \frac{y_{\mathrm{H_2O}} - \frac{1}{1+K_{\mathrm{eq},3}}}{\sqrt{\left(y_{\mathrm{H_2O}} - \frac{1}{1+K_{\mathrm{eq},3}}\right)^2 + \eta}}\right) \tag{107}$$

$$r_4^M = r_{4+}^M \cdot \left(0.5 + 0.5 \frac{y_{\mathrm{H_2O}} - \frac{1}{1+K_{\mathrm{eq},4}}}{\sqrt{\left(y_{\mathrm{H_2O}} - \frac{1}{1+K_{\mathrm{eq},4}}\right)^2 + \eta}}\right) + r_{4-}^M \cdot \left(0.5 - 0.5 \frac{y_{\mathrm{H_2O}} - \frac{1}{1+K_{\mathrm{eq},4}}}{\sqrt{\left(y_{\mathrm{H_2O}} - \frac{1}{1+K_{\mathrm{eq},4}}\right)^2 + \eta}}\right) \tag{108}$$

Here, r_{j+}^M and r_{j-}^M denote the forward and backward reaction rate of reaction j, respectively, and η is an adjustable parameter for the steepness of the sigmoid function. The value is set to $\eta = 1 \times 10^{-7}$, providing a fair trade-off between accuracy and numerical stability. However, the approximation of the original reaction

rates by a differentiable function gives rise to a new problem. In equations (105) to (108), the forward and backward reaction rates are both computed regardless of the actual composition of the gas. Therefore, terms like $\left(y_{\mathrm{CO_2}}^{(G)} - \frac{y_{\mathrm{CO}}^{(G)}}{K_{\mathrm{eq},1}}\right)$ (see eq. 101) yield negative values if $\frac{y_{\mathrm{CO}}^{(G)}}{y_{\mathrm{CO_2}}^{(G)}} > K_{\mathrm{eq},1}$. For non-integer values of the corresponding exponent m_O this becomes problematic because a solution exists only in complex space. To avoid this, the absolute values are used for calculation. However, since the absolute function is non-differentiable at $x = 0$, a differentiable approximation must be used again. The approximation function is exemplified in the following for the relevant term in equation 101:

$$y_{\mathrm{CO_2}}^{(G)} - \frac{y_{\mathrm{CO}}^{(G)}}{K_{\mathrm{eq},1}} \approx \sqrt{\left(y_{\mathrm{CO_2}}^{(G)} - \frac{y_{\mathrm{CO}}^{(G)}}{K_{\mathrm{eq},1}}\right)^2 + \eta}$$

Again, η is an adjustable parameter for the smoothness of the approximation and set to $\eta = 1 \times 10^{-7}$. Using similar approximations for equations 101 to 104, the original reaction rate equations are converted into differentiable functions, which are better suited for numerical integration. Additional problems may occur in the calculation of the ratios of mole fractions $y_i^{(G)}$. During the oxidation stage, the gas inside the reactor consists of only CO_2 and CO after the leftover gas from the reduction stage is purged. Thus, the denominator in equations (97) and (98) would become zero. The same is true for the denominators in equations (95) and (96) for the reduction stage. A machine epsilon is added to the denominator in equations (95) to (98) to avoid division by zero during simulation.

Nomenclature

Abbreviations		
CLC	Chemical looping combustion	
OSM	Oxygen storage material	
RWGS	Reverse water-gas shift	
RWGS-CL	Reverse water-gas shift chemical looping	
Symbols		
α	Reduction extent	–
ε	Void fraction	–
δ	Bubble fraction	–
η	Steepness parameter for sigmoid function	–
η_{eff}	Effectiveness factor for chemical reaction	–
μ	Dynamic viscosity	$\mathrm{Pa \cdot s}$
ν	Stoichiometric coefficient	–

ρ	Density	$\mathrm{kg \cdot m^{-3}}$
σ^M	Specific source term	$\mathrm{kg \cdot m^{-3} \cdot s^{-1}}$
c_t	Total concentration	$\mathrm{mol \cdot m^{-3}}$
c_p	Molar heat capacity	$\mathrm{J \cdot mol^{-1} \cdot K^{-1}}$
d	Diameter/particle and bubble size	m
$D_v^{(S)}$	Average vertical dispersion coefficient of the solids	$\mathrm{m^2 \cdot s^{-1}}$
E_A	Activation energy	$\mathrm{J \cdot mol^{-1}}$
g	Gravitational acceleration	$\mathrm{m \cdot s^{-2}}$
j	Diffusive flux	$\mathrm{kg \cdot m^{-2} \cdot s^{-1}}$
$K^{(be)}$	Gas interchange coefficient between bubble and emulsion phase	$\mathrm{s^{-1}}$
K_{eq}	Equilibrium constant	–
k^0	Pre-exponential factor in Arrhenius term	$\mathrm{mol \cdot kg_{OSM}^{-1} \cdot s^{-1}}$
L	Length/height	m
M	Molar mass	$\mathrm{kg \cdot mol^{-1}}$
m	Exponent for gas concentration in reaction rate	–
m_{OSM}	Mass of OSM in the reactor	kg
n	Exponent for solid concentration in reaction rate	–
R	Universal gas constant	$\mathrm{J \cdot mol^{-1} \cdot K^{-1}}$
r	Volumetric reaction rate	$\mathrm{mol \cdot m^{-3} \cdot s^{-1}}$
r^M	Specific reaction rate	$\mathrm{mol \cdot kg^{-1} \cdot s^{-1}}$
T	Temperature	K
t	Time	s
v	Velocity	$\mathrm{m \cdot s^{-1}}$
$v^{(G)}$	Superficial gas velocity	$\mathrm{m \cdot s^{-1}}$
$v^{(b)}$	Bubble phase gas velocity	$\mathrm{m \cdot s^{-1}}$
$v^{(e)}$	Emulsion phase gas velocity	$\mathrm{m \cdot s^{-1}}$
X_{OSM}	OSM utilization	–
x	Mole fraction	–
Y	Carbon or hydrogen content	–
y	Ratio of mole fractions	–
z	Space coordinate	m

References

[1] M. Wenzel, L. Rihko-Struckmann, K. Sundmacher, Thermodynamic Analysis and Optimization of RWGS Processes for Solar Syngas Production from CO_2, AIChE Journal 63 (2017) 15–22.

[2] Y. A. Daza, D. Maiti, R. A. Kent, V. R. Bhethanabotla, J. N. Kuhn, Isothermal reverse water gas shift chemical looping on $La_{0.75}Sr_{0.25}Co_{(1-Y)}Fe_YO_3$ perovskite-type oxides, Catalysis Today 258, Part 2 (2015) 691–698.

[3] M. Wenzel, N. Aditya Dharanipragada, V. V. Galvita, H. Poelman, G. B. Marin, L. Rihko-Struckmann, K. Sundmacher, CO Production From CO_2 via Reverse Water-Gas Shift Reaction Performed in a Chemical Looping Mode: Kinetics on Modified Iron Oxide, Journal of CO_2 Utilization 17 (2017) 60–68.

[4] W. C. Cho, D. Y. Lee, M. W. Seo, S. D. Kim, K. Kang, K. K. Bae, C. H. Kim, S. Jeong, C. S. Park, Continuous Operation Characteristics of Chemical Looping Hydrogen Production System, Applied Energy 113 (2014) 1667–1674.

[5] G. Wei, F. He, Z. Huang, A. Zheng, K. Zhao, H. Li, Continuous Operation of a 10 kW_{th} Chemical Looping Integrated Fluidized Bed Reactor for Gasifying Biomass Using an Iron-Based Oxygen Carrier, Energy & Fuels 29 (2015) 233–241.

[6] I. Ermanoski, N. P. Siegel, E. B. Stechel, A New Reactor Concept for Efficient Solar-Thermochemical Fuel Production, Journal of Solar Energy Engineering Transactions of the ASME 135 (2013).

[7] M. Welte, R. Barhoumi, A. Zbinden, J. R. Scheffe, A. Steinfeld, Experimental Demonstration of the Thermochemical Reduction of Ceria in a Solar Aerosol Reactor, Industrial & Engineering Chemistry Research 55 (2016) 10618–10625.

[8] S. F. Hakonsen, R. Blom, Chemical Looping Combustion in a Rotating Bed Reactor – Finding Optimal Process Conditions for Prototype Reactor, Environmental Science & Technology 45 (2011) 9619–9626.

[9] S. Zhang, R. Xiao, W. Zheng, Comparative study between fluidized-bed and fixed-bed operation modes in pressurized chemical looping combustion of coal, Applied Energy 130 (2014) 181–189.

[10] F. N. Ridha, D. Lu, A. Macchi, R. W. Hughes, Combined calcium looping and chemical looping combustion cycles with cao–cuo pellets in a fixed bed reactor, Fuel 153 (2015) 202–209.

[11] G. Voitic, S. Nestl, M. Lammer, J. Wagner, V. Hacker, Pressurized hydrogen production by fixed-bed chemical looping, Applied Energy 157 (2015) 399–407.

[12] T. Pröll, P. Kolbitsch, J. Bolhàr-Nordenkampf, H. Hofbauer, A Novel Dual Circulating Fluidized Bed System for Chemical Looping Processes, AIChE Journal 55 (2009) 3255–3266.

[13] A. Bischi, Ø. Langørgen, I. Saanum, J. Bakken, M. Seljeskog, M. Bysveen, J.-X. Morin, O. Bolland, Design Study of a 150 kW_{th} Double Loop Circulating Fluidized Bed Reactor System for Chemical Looping Combustion with Focus on Industrial Applicability and Pressurization, International Journal of Greenhouse Gas Control 5 (2011) 467–474.

[14] A. Abad, R. Pérez-Vega, L. F. de Diego, F. García-Labiano, P. Gayán, J. Adánez, Design and Operation of a 50 kW_{th} Chemical Looping Combustion (CLC) Unit for Solid Fuels, Applied Energy 157 (2015) 295–303.

[15] P. Ohlemüller, F. Alobaid, A. Gunnarsson, J. Ströhle, B. Epple, Development of a Process Model for Coal Chemical Looping Combustion and Validation Against 100 kW_{th} tests, Applied Energy 157 (2015) 433–448.

[16] S. Penthor, F. Zerobin, K. Mayer, T. Pröll, H. Hofbauer, Investigation of the Performance of a Copper Based Oxygen Carrier for Chemical Looping Combustion in a 120 kW Pilot Plant for Gaseous Fuels, Applied Energy 145 (2015) 52–59.

[17] C. Linderholm, M. Schmitz, P. Knutsson, A. Lyngfelt, Chemical-looping Combustion in a 100 kW Unit Using a Mixture of Ilmenite and Manganese Ore as Oxygen Carrier, Fuel 166 (2016) 533–542.

[18] Zhiquan Zhou, Lu Han, George M. Bollas, Overview of Chemical-Looping Reduction in Fixed Bed and Fluidized Bed Reactors Focused on Oxygen Carrier Utilization and Reactor Efficiency, Aerosol and Air Quality Research 14 (2014) 559–571.

[19] P. Heidebrecht, C. Hertel, K. Sundmacher, Conceptual Analysis of a Cyclic Water Gas Shift Reactor, International Journal of Chemical Reactor Engineering 6 (2008).

[20] F. Logist, J. Lauwers, B. Trigaux, J. F. van Impe, Model based optimisation of a cyclic reactor for the production of hydrogen, in: 21st European Symposium on Computer Aided Process Engineering, volume 29 of *Computer Aided Chemical Engineering*, Elsevier, Amsterdam and Oxford, 2011, pp. 457–461.

[21] P. Heidebrecht, K. Sundmacher, Thermodynamic Analysis of a Cyclic Water Gas-Shift Reactor (CWGSR) for Hydrogen

Production, Chemical Engineering Science 64 (2009) 5057–5065.

[22] D. Kunii, O. Levenspiel, Fluidized Reactor Models. 1. For Bubbling Beds of Fine, Intermediate, and Large particles. 2. For the Lean Phase: Freeboard and Fast Fluidization, Industrial & Engineering Chemistry Research 29 (1990) 1226–1234.

[23] L. E. Baur, A. Z. Glaessner, , Phys. Chem. 43 (1903) 354–368.

[24] C. Hertel, P. Heidebrecht, K. Sundmacher, Experimental Quantification and Modelling of Reaction Zones in a Cyclic Watergas Shift Reactor, International Journal of Hydrogen Energy 37 (2012) 2195–2203.

[25] H. Y. Sohn, On the rate expressions for "reversible" gas–solid reactions, Metallurgical and Materials Transactions B 45 (2014) 1600–1602.

[26] A. Wolf, A. Jess, C. Kern, Syngas Production via Reverse Water-Gas Shift Reaction over a Ni-Al_2O_3 Catalyst: Catalyst Stability, Reaction Kinetics, and Modeling, Chemical Engineering & Technology 39 (2016) 1040–1048.

[27] C. L. Yaws, Thermophysical Properties of Chemicals and Hydrocarbons, William Andrew, Norwich, N.Y., 2008.

[28] B. Moghtaderi, Review of the recent chemical looping process developments for novel energy and fuel applications, Energy & Fuels 26 (2012) 15–40.

[29] W. M. Haynes, CRC Handbook of Chemistry and Physics, CRC Press, Hoboken, 95th edition, 2014.

[30] D. Geldart, Types of Gas Fluidization, Powder Technology 7 (1973) 285–292.

[31] D. Kunii, O. Levenspiel, Fluidization Engineering, Butterworth-Heinemann series in chemical engineering, Wiley, New York, 2nd edition, 1991.

[32] V. Gesellschaft, VDI-Wärmeatlas, Springer Berlin Heidelberg, Wiesbaden, 10th edition, 2005.

[33] J. R. Fernández, J. C. Abanades, Conceptual Design of a Ni-based Chemical Looping Combustion Process Using Fixed-beds, Applied Energy 135 (2014) 309–319.

[34] V. Spallina, P. Chiesa, E. Martelli, F. Gallucci, M. C. Romano, G. Lozza, M. van Sint Annaland, Reactor Design and Operation Strategies for a Large-scale Packed-bed CLC Power Plant with Coal Syngas, International Journal of Greenhouse Gas Control 36 (2015) 34–50.

[35] A. A. M. Parra, C. Asmanoglo, D. W. Agar, Cyclic Steady-State Behavior and Optimization of a Fixed-Bed Adsorptive Reactor for the Reverse Water-Gas Shift Reaction, Chemical Engineering & Technology (2016).

[36] P. Trambouze, J.-P. Euzen, Chemical Reactors: From Design to Operation, Editions TECHNIP, Paris, revised edition, 2004.